ACS Catalysis

Perspective

pubs.acs.org/acscatalysis

Recent Advances of Lanthanum-Based Perovskite Oxides for Catalysis

Huiyuan Zhu,*[,†] Pengfei Zhang,[†] and Sheng Dai*[,†,‡]

[†]Chemical Sciences Division, Oak Ridge National Laboratory, Oak Ridge, Tennessee 37831, United States

[‡]Department of Chemistry, University of Tennessee, Knoxville, Tennessee 37996, United States

ABSTRACT: There is a need to reduce the use of noble metal elements—especially in the field of catalysis, where noble metals are ubiquitously applied. To this end, perovskite oxides, an important class of mixed oxide, have been attracting increasing attention for decades as potential replacements. Benefiting from the extraordinary tunability of their compositions and structures, perovskite oxides can be rationally tailored and equipped with targeted physical and chemical properties—for example, redox behavior, oxygen mobility, and ionic conductivity—for enhanced catalysis. Recently, the development of highly efficient perovskite oxide catalysts has been extensively studied. This perspective article summarizes the recent development of lanthanum-based perovskite oxides as advanced catalysts for both energy conversion applications and traditional heterogeneous reactions.

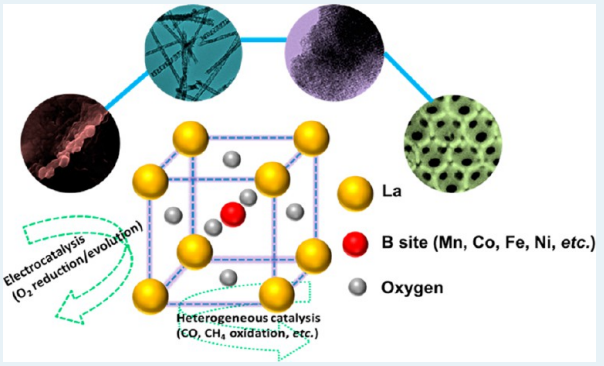

KEYWORDS: *perovskite oxides, electrocatalysis, oxygen reduction/evolution reaction, heterogeneous catalysis, CO oxidation, methane oxidation*

1. INTRODUCTION

Perovskites have emerged as an important new class of materials in the mixed-oxide family because of their exceptional thermal stability, electronic structure, ionic conductivity, electron mobility, and redox behavior.[1−4] They have the general formula ABO_3, where A is a typical lanthanide, alkaline, or alkaline-earth cation and B is any one of a variety of transition metal cations, such as Mn, Co, Fe, Ni, Cr, and Ti. Figure 1 shows an ideal cubic perovskite oxide unit cell from the space group *Pm*3*m* in which the larger cation A coordinates with 12 oxygen anions, and the smaller cation B coordinates with 6 oxygen anions. In reality, a distortion of the crystalline structure exists as a result of the insertion of multiple A or B cations with different sizes and valences. Oxygen nonstoichiometry including both oxygen deficiency and oxygen excess is common, in which the overall charges of the A and B cations are less or greater than the charges of the oxygen anions (six). This results in a more general formula $A_{1-x}A'_xB_{1-y}B'_yO_{3\pm\delta}$, where "+" denotes oxygen excess and "−" denotes oxygen deficiency. More importantly, as a benefit of the numerous possible substitutions at both A and B sites, perovskites offer great flexibility with regard to the tailoring and tuning of their physi-chemical properties. For example, substituting B cations with a reducible early transition metal—such as Co, Mn, or Fe—provides redox active sites to facilitate catalytic reactions, including CO oxidation[5,6] and NO oxidation.[7] Moreover, with a rational substitution of A or B cations with other elements (e.g., Sr, Ce, Ba), oxygen vacancies can be introduced to the structure to facilitate oxygen transfer and thus increase oxygen mobility.[8−11] In fact, around 90% of the metallic elements from the periodic table can form perovskite oxide structures, giving rise to a broad possibility for enabling tunable electronic and geometric synergies between different substitutes.

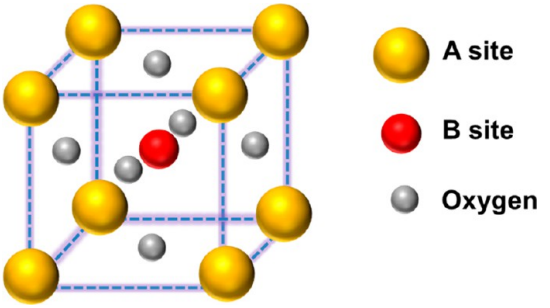

Figure 1. Schematic illustration of an ideal ABO_3 perovskite unit cell.

The broad family of perovskite oxides and the consequent wide range of substitutions give rise to the great flexibility of the perovskite band structure, which in turn has a significant influence on perovskite catalytic performance. The cations on the B sites were found to play essential roles in altering the electronic structure of the perovskite oxides, thus modifying the

Received: July 31, 2015
Revised: September 19, 2015

ACS Publications © XXXX American Chemical Society

DOI: 10.1021/acscatal.5b01667
ACS Catal. 2015, 5, 6370−6385

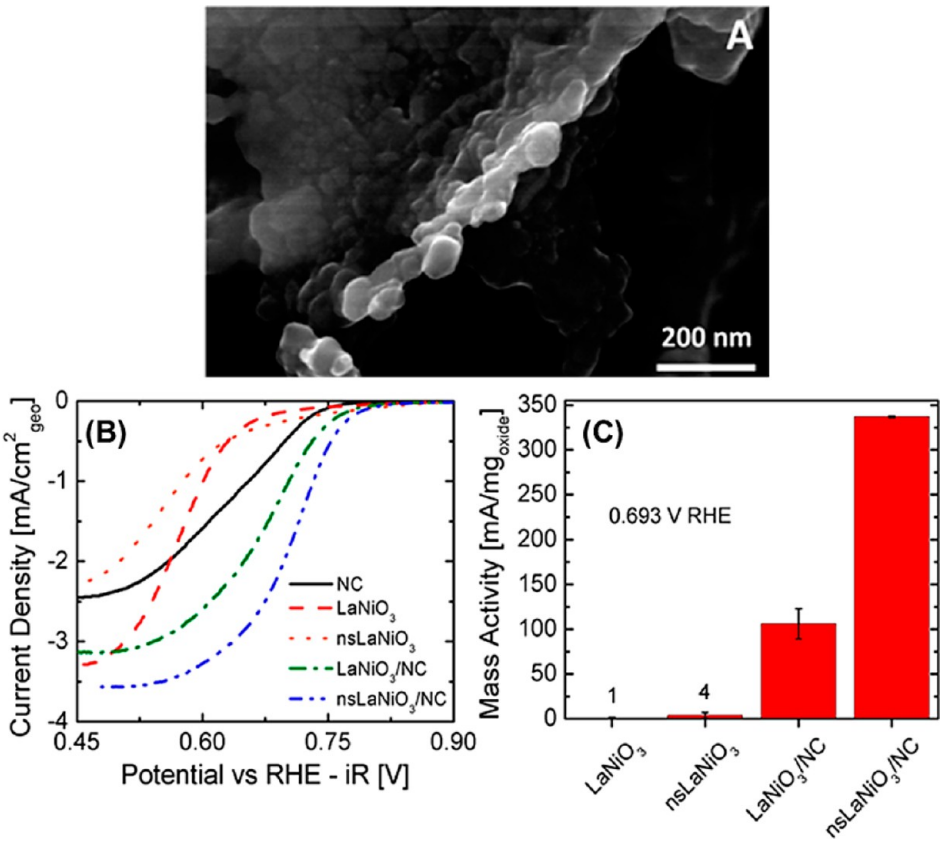

Figure 2. (A) Scanning electron microscopy image of calcined $LaNiO_3$ after freeze-drying. (B) ORR polarization curves of NC, unsupported $LaNiO_3$, nsLaNiO$_3$, supported $LaNiO_3$/NC and nsLaNiO$_3$/NC in O_2-saturated 0.1 M KOH at 1600 rpm. (C) Mass activities of NC, unsupported $LaNiO_3$, nsLaNiO$_3$, supported $LaNiO_3$/NC, and nsLaNiO$_3$/NC at 0.693 vs the RHE.[38]

catalytic process. This effect was mainly controlled by the strength of the bond between the B-site species and the oxygenated species.[12−15] Because of the minor effects of the A site cations of various lanthanides on catalysis, lanthanum-based (La-based) perovskite oxides have been the most frequently studied and have demonstrated remarkable performance in different types of catalysis.[3,4,16] Because the family of perovskite oxides is so large, this Perspective will focus only on La-based perovskite oxides, namely, $LaBO_3$ (B = Fe, Co, Ni, Cr, Mn, Cu, etc.) and their partial substitutions. This perspective will cover the most recent advances in La-based perovskite oxides for catalytic applications—including their synthesis, characterization, and catalytic performance—for reactions involved in electrochemistry, such as oxygen reduction reaction (ORR) and oxygen evolution reaction (OER), and for reactions involved in gas−solid-phase heterogeneous catalysis, such as carbon monoxide (CO) oxidation, methane oxidation, methanol, and NO conversion.

2. LA-BASED PEROVSKITES AS ELECTROCATALYSTS FOR OXYGEN REDUCTION REACTIONS

The ORR in alkaline media acts as the cathode reaction in a range of electrochemical energy converting devices, including metal-air batteries, solid oxide fuel cells, and alkaline fuel cells.[17] The ORR in alkaline media follows either a direct four-electron pathway eq 1 or a two-electron pathway with HO_2^- generated as the intermediate (eq 2a). The sluggish ORR kinetics makes it the main obstacle to maximizing energy output in these advanced energy schemes. Conventionally, nanomaterials based on noble metals, including Pt, Pd, Au, and their alloy derivatives, are implemented as ORR catalysts to speed up the cathode kinetics and lower the accompanying overpotentials in these energy devices.[18−20] It is worth noting that the high cost and low abundance associated with these noble-metal-based nanocatalysts hamper the commercialization of these electrochemical energy devices.

$$O_2 + 2H_2O + 4e^- \rightarrow 4OH^- \quad (1)$$

$$O_2 + H_2O + 2e^- \rightarrow HO_2^- + OH^- \quad (2a)$$

$$HO_2^- + H_2O + 2e^- \rightarrow 3OH^- \quad (2b)$$

Since their debut in 1970s as potential ORR catalysts,[21] La-based perovskite oxides have become one of the hottest topics in the field of electrocatalysis. Unlike noble metal nanocatalysts, La-based perovskite oxides demonstrate their intriguing performance in ORR catalysis, preferably in alkaline media, because the redox couple near the oxygen reduction potential provided by the B site—normally a Co, Mn, or Fe cation—is unstable in an acid environment. Nevertheless, these cations are quite stable in alkaline media and usually display a well-defined redox couple near the oxygen reduction potential to facilitate oxygen reduction.[22] Various La-based perovskite oxides have been studied, including $LaCoO_3$, $LaFeO_3$, and $LaNiO_3$, and they show promising performance in ORR in alkaline media.[23−28] The activity of these La-based perovskite oxides strongly correlates with the covalent bond strength between B-site cations and the oxygenated species. A volcano plot of ORR catalytic activity versus B−OH bond strength was proposed on the basis of the observation that the activity increases with a

DOI: 10.1021/acscatal.5b01667
ACS Catal. 2015, 5, 6370−6385

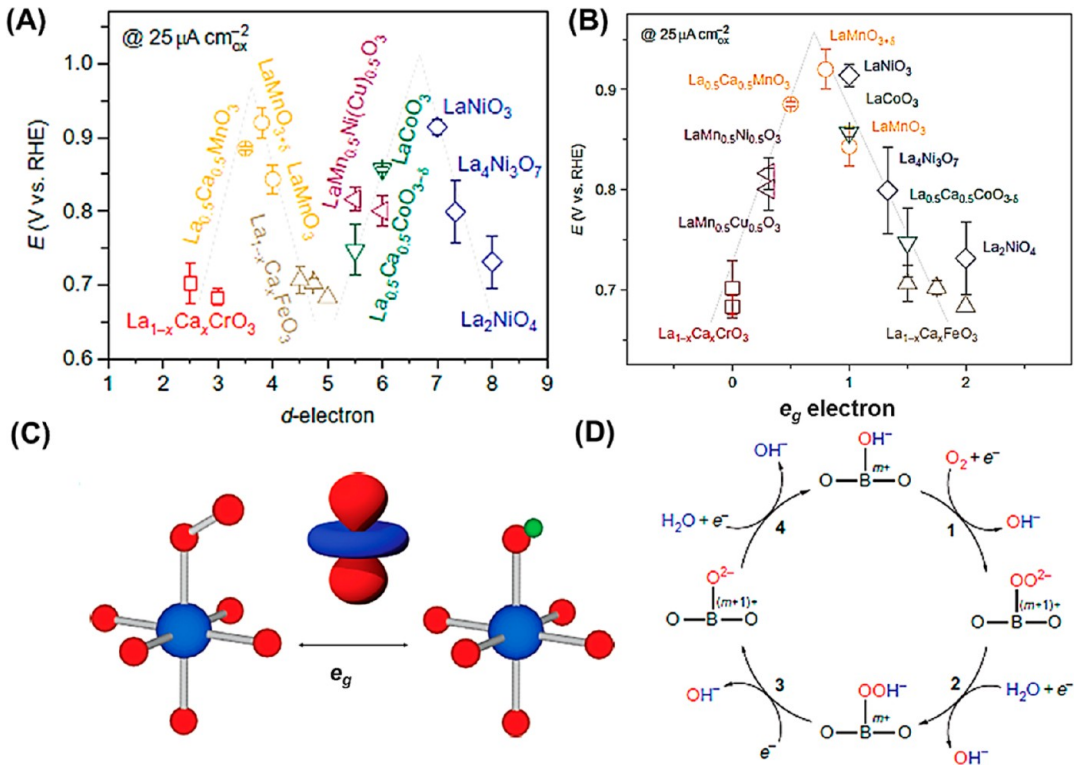

Figure 3. (A) M-shaped relationship between the potential at 25 μA cm$^{-2}_{ox}$ vs the d-electron number of the perovskite oxides. (B) Potentials at 25 μA cm$^{-2}_{ox}$ as a function of e_g orbital in perovskite-based oxides. (C) The shape of the e_g electron points directly toward the surface oxygen atom (red: oxygen; blue: B-site; green: hydrogen). (D) Proposed ORR mechanism on perovskite oxide surface. Reprinted with permission from ref 39. Copyright 2011 Nature Publishing Group.

higher occupancy of antibonding σ^* orbitals. Although the La-based perovskite oxides have shown great potential as electrocatalysts for ORR, their low intrinsic electron conductivity remains a hurdle. To fully reveal their electrochemical behavior, carbon is often used as a conductive additive.[29] Fundamentally, the exact ORR pathway in La-based perovskite oxides is still under debate. Both the pseudo 4e$^-$[23] and the series 2e$^-$[30,31] pathways have been reported in La-based perovskite oxides, and the reaction process has been found to be largely dependent on the amount of perovskite loading, the conductive additives, and the oxide type.[32]

2.1. B-Site Substitution Effect on ORR. As mentioned above, the choice of B-site cations correlates strongly with their ORR performance because of the possible formation of redox couples near the oxygen reduction region[33] and the tunable bond strength of B−OH. To understand the B-site effect on the ORR, a systematic study of different $LaBO_3$ compounds is needed. Forsyth et al. reported the synthesis of $LaMO_3$ (M = Ni, Co, Fe, Mn, and Cr) through a combined ethylenediaminetetraacetic acid (EDTA)-citrate complexation process with La-nitrate and a transition-metal nitrate as the metal precursors, followed by calcination at 1000 °C in air to remove the residue and further crystallize the product into the perovskite structure.[23] Extending the synthesis to $LaNi_{0.5}M_{0.5}O_3$ (M = Ni, Co, Fe, Mn, and Cr) was successfully achieved by varying the Ni-to-M precursor ratio. The as-made La-based perovskite oxides were first mixed with carbon to increase the electron conductivity. Then the electrocatalysis of the ORR was systematically studied in these materials. Among these perovskite oxides, $LaCoO_3$ demonstrated the highest ORR current density and lowest overpotential in 0.1 M KOH.

The ORR activity with the presence of two transition metals on the B site was further investigated. Doping of manganese (Mn) at a ratio of 0.5 into the Ni-site of $LaNiO_3$ substantially improved the performance toward ORR. Furthermore, a four-electron pathway was observed on these La-based perovskite oxide surfaces. The ORR kinetics was improved in the order of $LaNi_{0.5}Fe_{0.5}O_3$, $LaNi_{0.5}Co_{0.5}O_3$, $LaNi_{0.5}Cr_{0.5}O_3$, and $LaNi_{0.5}Mn_{0.5}O_3$.

Traditionally, the perovskite oxides are synthesized through either high-energy ball milling[34,35] or high-temperature calcination.[23,36,37] Unfortunately, these processes lead to the formation of a micron-sized product with a low surface area (<10 m^2 g^{-1}). To increase the number of active sites per unit of geometric area and thus reduce the overpotential associated with ORR, La-based perovskite oxides with high surface areas are highly desirable. Thus, an intensive effort was initiated to develop nanostructured perovskite oxides. Nanostructured $LaNiO_3$ (ns$LaNiO_3$) was recently prepared via the lyophilization of a frozen mixed La^{3+} and Ni^{2+} hydroxide thin film, followed by calcination at 700 °C.[38] This rapid "freeze-drying" method effectively mitigated the aggregation of the $LaNiO_3$, allowing the formation of nanostructures (Figure 2A). Supported on nitrogen-doped carbon (NC), this ns$LaNiO_3$ demonstrated largely improved ORR activity (Figure 2B) with positively shifted onset and half-wave potentials and a much higher mass activity at 0.693 V vs a reversible hydrogen electrode (RHE), compared with its bulk counterpart (Figure 2C). The improved performance compared with the bulk was attributed to the high surface area and abundant catalytic active sites in the crystalline ns$LaNiO_3$.

DOI: 10.1021/acscatal.5b01667
ACS Catal. 2015, 5, 6370−6385

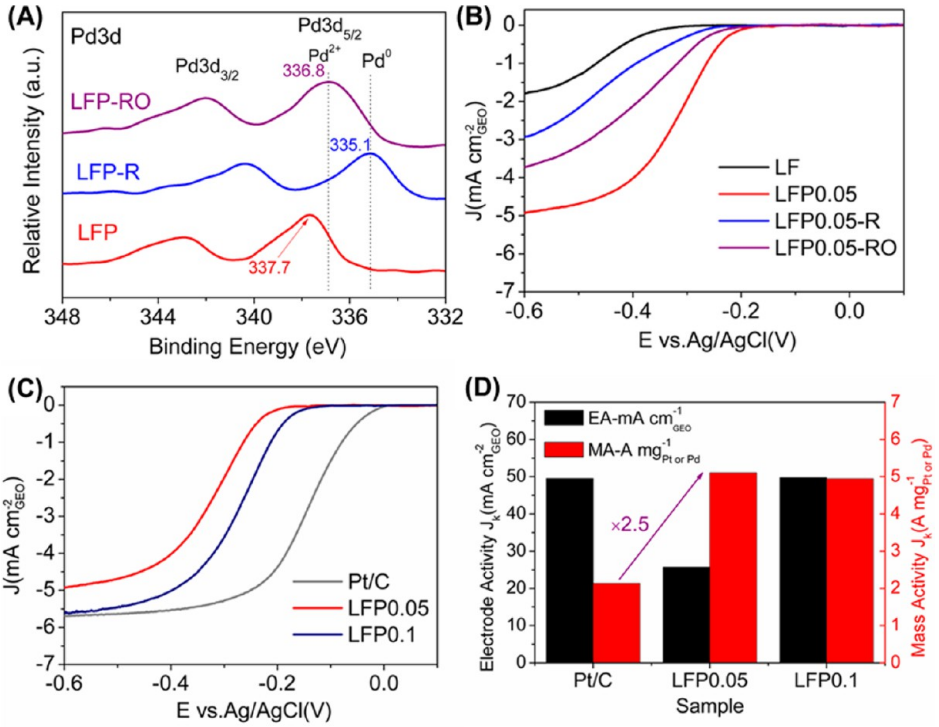

Figure 4. (A) X-ray photoelectron spectroscopy spectra of Pd for LFP0.05, LFP0.05R and LFP0.05RO. (B) ORR polarization curves of LF, LFP0.05,LFP0.05R, LFP0.05RO. (C) Commercial 20 wt % Pt/C, LFP0.05, and LFP0.1 in O_2-saturated 0.1 M KOH with the rotating disk at 1600 rpm at a scan rate of 5 mV s^{-1}. (D) ORR electrode activity (EA) and mass activity (MA) of LFP0.05, LFP0.1, and commercial 20 wt % Pt/C at −0.6 V.[50]

Although La-based perovskite oxides have repeatedly been reported as potential ORR catalysts, there is little fundamental understanding of the ORR mechanism on these oxide surfaces; thus the need to identify the unique catalytic parameter that governs ORR activity is urgent. Until recently, this activity descriptor for La-based perovskite oxides had been clearly revealed by Yang et al. based on a molecular-orbital approach.[39] A total of 15 La-based perovskite oxides—including $La_{1-x}Ca_xMnO_3$ (x = 0, 0.5), $La_{0.5}Ca_{0.5}CrO_3$, $LaNi_{0.5}Mn_{0.5}O_3$, $LaCu_{0.5}Mn_{0.5}O_3$, $LaCrO_3$, $La_4Ni_3O_{10}$, $LaNiO_3$, $LaMnO_3$, La_2NiO_4, $La_{1-x}Ca_xFeO_3$ (x = 0, 0.25, 0.5), $La_{1-x}Ca_xCoO_3$ (x = 0, 0.5) and $La_3Ni_2O_7$—were prepared through the coprecipitation of La-, alkaline earth- (Ca), and transition-metal- (Mn, Cr, Ni, Cu, Fe, Co) nitrates in Milli-Q water, followed by calcination at high temperature (≥800 °C) in both inert (argon) and air atmospheres. On the basis of the fact that the d-electron on the B site resembles the antibonding occupation in the B−O bond, ORR activities in 0.1 M KOH on these La-based perovskite oxide surfaces were correlated with their d-electron number per B-site cation. Consequently, an M-shaped relationship was obtained, with the maximum performance achieved on La-based perovskite oxide surfaces with d^4 and d^7 configurations (Figure 3A). This d-electron effect was also observed in gas-phase CO and hydrocarbon oxidation catalysis on perovskite oxides.[40,41] To further investigate the d-electron effect, a volcano-shaped behavior plot was attained by correlating the e_g electron (σ^* orbital occupation) with ORR activity, as shown in Figure 3B. The e_g orbital overlaps strongly with the O-2p_σ orbital (Figure 3C), determining the B−O bond strength during the chemisorption of oxygenated species in ORR. The best performance toward ORR catalysis on these perovskite oxides is achieved when e_g is close to 1 (Figure 3B). This observation follows the Sabatier principle, which is that the interaction between the adsorbate and the catalyst should be neither too strong nor too weak.[42] It is also similar to the d-band theory, proposed for metal catalysts during ORR, that a balance between the adsorption and the desorption of the oxygenated species is critical to optimized ORR performance.[43] Too little σ^* orbital occupation (e_g < 1) or too much occupation (e_g > 1) results in interactions with the oxygenated species that are either too strong or too weak. Consequently, optimized ORR catalysis on perovskite oxides proceeds at an e_g number close to 1.

The authors proposed an explanation of the ORR mechanism on perovskite oxides accordingly (Figure 3D), which constitutes surface hydroxide (OH^-) displacement (step 1), surface peroxide formation (step 2), surface oxide formation (step 3), and surface OH^- regeneration (step 4). The presence of a single σ^* electron (e_g = 1) promotes the replacement of OH^- with O_2 by destabilizing the B−OH^- bond. This work innovatively identified the relationship between ORR activity on perovskite oxides and their electronic structure, providing important insights and design rules for oxide catalysts. The e_g number, in particular, serves as the effective activity descriptor for ORR catalysis on perovskite oxides. On the basis of this rule, several advanced La-based perovskite oxides (e.g., $LaNi_{1-x}Fe_xO_3$,[44] $LaMnO_3$[45,46]) have been identified as promising electrocatalysts for ORR.

The insights gained from these studies have provoked extensive research into the effects of substitution of B-site cations to tailor the oxidation state of the B cation and e_g occupancy to achieve favorable kinetics for ORR. Most of these studies are based on the use of a 3d-transition metal as the B site cations or substitutions.[23,47] The presence of two or more

DOI: 10.1021/acscatal.5b01667
ACS Catal. 2015, 5, 6370−6385

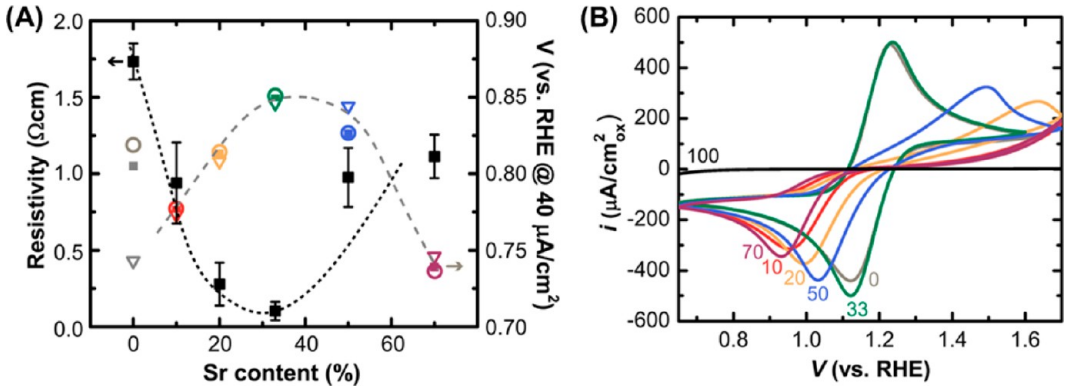

Figure 5. (A) Left axis: the resistivity vs strontium content in LSMO; right axis: the voltage at 40 μA/cm^2 of capacitance-corrected current from the fifth cycle of initial cyclic voltammetry (CV) measurements (open circle), subsequent chronoaperometry (solid square), and CV measurements following sweeping to oxidative potentials (open triangles). (B) CV at 10 mV/s on LSMO films for 10 mM $[Fe(CN)_6]^{3-/4-}$ in argon-saturated 0.1 M KOH.[58]

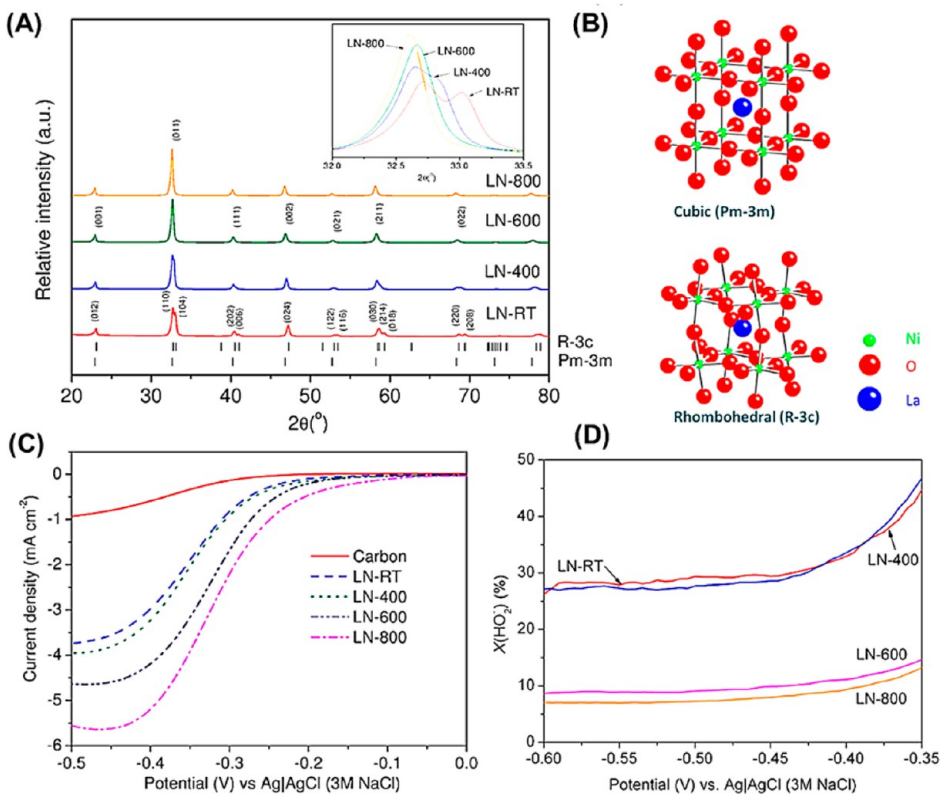

Figure 6. (A) X-ray diffraction patterns of LN-RT, LN-400, LN-600, and LN-800. (Inset: close look at 32° for $LaNiO_3$ perovskites with various crystal structures). (B) Crystal structure of rhombohedral and cubic $LaNiO_3$ perovskites. (C) ORR polarization curves for LN-RT, LN-400, LN-600, and LN-800 at 1600 rpm in O_2-saturated 0.1 M KOH at 5 mV s^{-1}. (D) Peroxide yield during ORR on LN-RT, LN-400, LN-600, and LN-800 surfaces.[62]

different B-site cations may introduce additional synergistic effects into the perovskite structure. For instance, the partial substitution of iron for Mn in $LaMnO_3$ significantly stabilizes the $LaMnO_3$ structure.[48,49] Recently, a similar strategy has been applied to replace some of the B-site cations with the 4d-transition metal palladium (Pd) to exploit the tuning effect of the perovskite structure on Pd, especially the tuning of the oxidation state of Pd.[50] The compounds $LaFe_{0.95}Pd_{0.05}O_3$ (LFP0.05) and $LaFe_{0.9}Pd_{0.1}O_3$ (LFP0.1) were synthesized according to a combined EDTA-citrate complexing sol–gel approach with metal nitrates as the precursors. The oxidation state of Pd is controlled by post-thermal treatment either in a reducing atmosphere to yield Pd^0 (LFP0.05R) or in air to produce Pd^{2+} (LFP0.05RO). The valence state of Pd in LFP0.05 presents a mixture of Pd^{3+} and Pd^{4+} in the perovskite structure (Figure 4A). The ORR activity in an alkaline electrolyte follows the order of $LaFeO_3$ (LF) < LFP0.05R< LFP0.05RO < LFP0.05, suggesting an increased intrinsic ORR activity on the Pd surface with higher oxidation states (perovskite-type ionic $Pd^{3+/4+}$) (Figure 4B). The activity of the LFP catalyst can be further improved by increasing the Pd ratio (Figure 4C). By normalizing the kinetic current to the amount of the noble metal, the LFP0.1 catalyst shows a higher mass activity than the benchmark platinum catalyst (Figure

DOI: 10.1021/acscatal.5b01667
ACS Catal. 2015, 5, 6370–6385

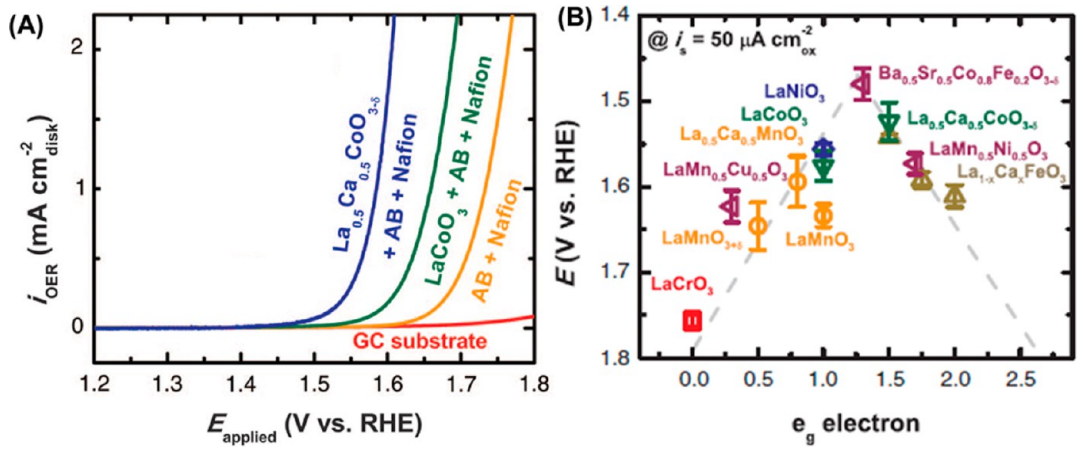

Figure 7. (A) OER polarization curves of glassy carbon (GC) electrode, acetylene black (AB), and Nafion-modified GC electrode, $LaCoO_3$ and $La_{0.5}Ca_{0.5}CoO_{3-\delta}$ thin films with AB and Nafion on GC. (B) The relationship between the OER activity, defined by the overpotentials at the current density of 50 μA cm$^{-2}_{ox}$, and the e_g occupancy of the transition metal (B in ABO_3). Reprinted with permission from ref 71. Copyright 2011 American Association for the Advancement of Science.

4D). The enhanced performance can be attributed to the synergistic effect between Pd and the perovskite structure. With the presence of $Pd^{3+/4+}$ on the B site, the e_g filling in perovskite is close to 1, and at the same time, the d-band center of Pd is downshifted by the high valence state to facilitate ORR catalysis.

2.2. A-Site Substitution Effect on ORR. Partial substituting La (3+) with an alkaline earth element (Ca^{2+} or Sr^{2+}) or a lanthanide with a different valence (Ce^{4+}) at the A site introduces oxygen nonstoichiometry into the perovskite structure, leading to an improved oxygen mobility.[1,28,51,52] Owing to the matched atomic size, strontium (Sr) is commonly doped with La on the A site, forming a $La_{1-x}Sr_xMO_3$ (M = Fe, Co, Mn) type of structure.[53−55] The substitution of La (3^+) with divalent Sr (2^+) results in cation vacancies and the formation of high-valence M cations to facilitate oxygen and electron transfer, making this structure a promising candidate for catalyzing ORR in alkaline media.[56] Tulloch et al. reported that Sr-dependent ORR performance in 1 M KOH with $La_{0.4}Sr_{0.6}MnO_3$ achieved the highest activity among all the $La_{1-x}Sr_xMnO_3$ compounds (LSMOs) studied.[57] Recently, Yang et al. explained the Sr-dependent ORR activity in LSMO on the basis of the study of a thin-film single crystal (001)-oriented epitaxial LSMO surface.[58] The ORR activity of LSMO was found to follow the reserve order of resistivity; LSMO with a 33% concentration of Sr reached the highest activity and lowest resistivity (Figure 5A), demonstrating the effect of the Sr doping on the conductivity. The intrinsic Sr effect was further investigated and ascribed to the ability to transfer electrons near the O_2/OH^- redox potential (1.23 V vs RHE). The well-defined redox couple at 1.2 V vs RHE in $[Fe(CN)]^{3-/4-}$ obtained on LSMO with 33% Sr indicates the favorable kinetics for electron transfer near the O_2/OH^- equilibrium region (Figure 5B).

2.3. Crystalline Structure Effect on ORR. The effect of the crystalline structure of the electrocatalyst has been highlighted by many theoretical and experimental investigations. Different crystalline structures were found to be critical in tailoring the electronic and geometric structures of electrocatalysts to influence their catalytic performance, especially for ORR.[59−61] The crystalline structure of La-based perovskite oxides also plays a role in influencing ORR. Zhou et al. synthesized $LaNiO_{3-\delta}$ with different crystal structures by heating premade $LaNiO_{3-\delta}$ powders (LN-RT) at 400 °C (LN-400), 600 °C (LN-600) and 800 °C (LN-800).[62] The LN-RT and LN-400 adopted a rhombohedral structure, whereas LN-600 and LN-800 formed a cubic structure. This phase transformation was evidenced by the merged peaks at 32° in LN-600 and LN-800 (Figure 6A). Both the Ni−O bond length and O−Ni−O bond angle increased with elevated temperature, releasing the lattice distortion in the rhombohedral structure (Figure 6B). The ORR activity also increased simultaneously with the temperature increase (Figure 6C). A four-electron reduction of O_2 into OH^- on LN-600 and LN-800 was confirmed by the detection of less than 10% HO_2^- on a rotating ring-disk electrode (Figure 6D). The slight elongation of the Ni−O bond in the cubic structure may provide favorable oxygen chemisorption to facilitate ORR. A similar strategy has been applied to the $La_{1-x}Sr_xMnO_3$ (LSM) system.[63] With the annealing temperature ranging from 650 (LSM650), through 750 (LSM750) to 800 °C (LSM800), the final crystal structures were identified as tetragonal, cubic, and orthorhombic, respectively, as a result of the lattice strain effect and anisotropic growth. The tetragonal LSM650 demonstrated the best ORR catalytic performance owing to the synergistic effect between the unit cell volume and the crystallinity. Note that although the crystalline structure effect of La-based perovskite oxides on ORR has been reported, details of the study of the synergy between the electronic structure and the crystalline phase remain insufficient and are highly desirable to provide insights into perovskite catalysis.

3. LA-BASED PEROVSKITES AS ELECTROCATALYSTS FOR OXYGEN EVOLUTION REACTION

The OER, which generates molecular oxygen via a four-electron reverse process of the ORR, is involved in many important energy conversion schemes, including the alkaline water-splitting cell and the charge process of aqueous metal−air batteries eq 3.[64−66] A similar process takes place in the nonaqueous lithium−air (Li−air) battery eq 4. Hampered by multiple electron transfers and oxygen−oxygen bond formation, slow kinetics and large overpotentials are often associated with OER. To expedite the reaction, ruthenium oxide (RuO_2) and iridium oxide (IrO_2) are commonly used as

DOI: 10.1021/acscatal.5b01667
ACS Catal. 2015, 5, 6370−6385

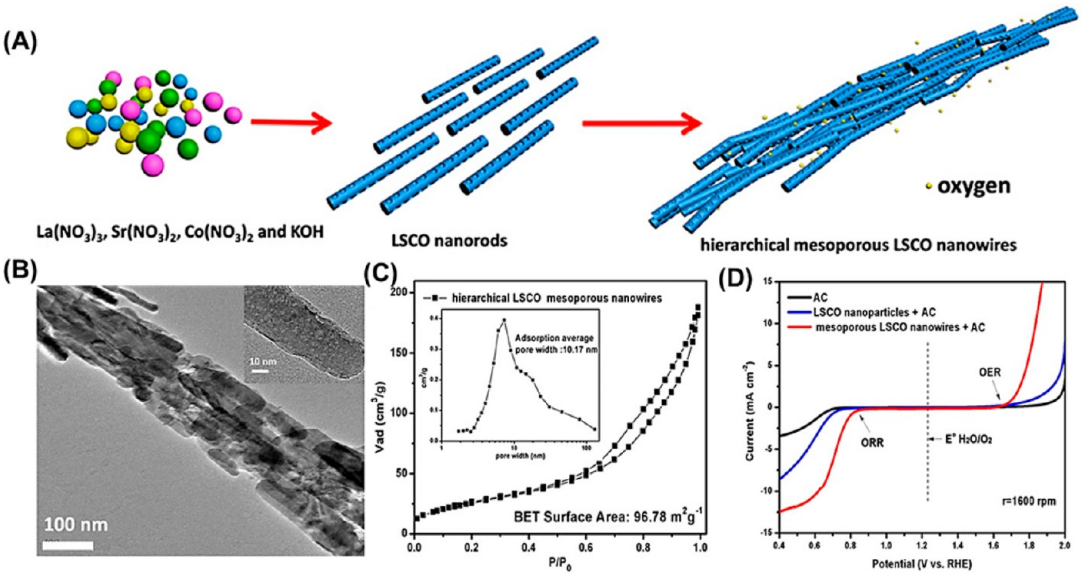

Figure 8. (A) Schematic illustration of the construction of the hierarchical mesoporous LSCO NWs. (B) TEM image of the hierarchical mesoporous LSCO NWs (inset: a single porous LSCO NR). (C) Nitrogen adsorption and desorption isotherms and pore size distribution (inset). (D) ORR and OER polarization curves of AC, LSCO NPs, and LSCO NWs + AC on glassy carbon electrodes at 1600 rpm rotation rates in O_2-saturated 0.1 M KOH with a can rate of 5 mV s^{-1}. Reprinted with permission from ref 83. Copyright 2012 National Academy of Sciences, U.S.A.

state-of-the-art catalysts for the electrochemical production of oxygen.[67−69] Despite their satisfying performance toward OER catalysis on RuO_2 and IrO_2 catalysts, the high cost and scarcity of these materials prevent their wide application in both water-splitting cells and metal−air batteries.

$$4OH^- \rightarrow O_2 + 2H_2O + 4e^- \quad (3)$$

$$Li_2O_2 \rightarrow 2Li^+ + O_2 + 2e^- \quad (4)$$

Since its first isolation as an electrocatalyst in 1980s, lanthanum nickelate ($LaNiO_3$) was discovered demonstrating an encouraging activity toward OER in alkaline media.[14,70] Similar to the case of ORR catalysis, the transition metal ions (e.g., Fe, Co, Mn, and Ni) at the B site play an important role, as the various valence states determine the adsorption and desorption of hydroxide ions. Generally, the occupancy of the antibonding orbitals (σ^*) in the B−OH bond decreases with a higher valence state (fewer d-electrons), leading to strong adsorption of OH on the B site.[14] More specifically, Yang et al. demonstrated the design principle of OER catalysts based on a molecular orbital bonding framework in alkaline solution.[71] Starting from the active OER catalysts $LaCoO_3$ and $La_{0.5}Ca_{0.5}CoO_{3-\delta}$ (Figure 7A), they systematically studied OER catalysis on a group of perovskite transition metal oxides and generated a volcano-type relationship describing the activity as a function of e_g filling of B-site cations (Figure 7B). Unlike in previously proposed reaction descriptors (3d electrons),[72,73] they successfully identified the importance of e_g and separated it from t_{2g} in d electrons. The relationship between the overpotentials during OER and the number of e_g electrons is shown in Figure 7B. On the left side of the volcano plot, the e_g occupation is small and the reaction is limited by the slow desorption of the OH and its derivatives during OER; on the right side, the number of e_g electrons is large and the limiting step is the slow adsorption of the reactants. Therefore, the perovskite oxides can achieve an enhanced intrinsic OER activity with $e_g = 1$ to balance the adsoprtion and desorption of the reactants and intermediates. Following this design rule for La-based perovskite oxides, several active OER electrocatalysts were identified and studied both experimentally and via ab initio caculations.[74,75]

To optimize OER catalysis on La-based perovskite oxides, an electrocatalyst with high surface area, which could provide a high accessibility of catalytically active sites per the geometric area, is necessary. Along with the active catalyst design—to accommodate the insoluble discharge products (Li_2O_2 and Li_2O) in a nonaqueous Li−air battery and to facilitate O_2 diffusion—the porous cathode structure is believed to play a key role in determing the mass and electron transport during the OER process.[76,77] In light of recent advances in the synthesis of well-defined, porous nanostructured La-based perovskite oxides,[78,79] the development of both active OER and bifunctional OER/ORR catalysts has been constantly revisited.[80−82] To construct a porous structure in perovskite and thus enhance the mobility of oxygen, $La_{0.5}Sr_{0.5}CoO_{3-\delta}$ (LSCO) nanowires (NWs) with a unique hierarchical mesoporous structure were prepared via a multistep micro-emulsion in an alkaline solution with La, Sr, and cobalt (Co) nitrates as the metal precursors, followed by high-temperature annealing.[83] During the synthesis, the metal precursors first decomposed and crystallized into LSCO nanorods (NRs). The LSCO NRs served as a template to mediate the oriented attachment of the NRs to form the hierarchical mesoporous structured LSCO NWs (Figure 8A). This porous hierarchical structure was confirmed by transmission electron microcopy (TEM) imaging (Figure 8B). The inset in Figure 8B shows the corresponding N_2 adsorption−desorption isotherms (Figure 8C) and Barrett−Joyner−Halenda pore-size distributions (inset of Figure 8C). Slit-shaped pores with an average size of 10.17 nm and a specific surface area of 96.78 m^2/g were observed in the structure. This porous structure was found to be essential to the oxgyen electrochemistry. Both ORR and OER activity was studied on these LSCO NWs, and the LSCO NWs showed much better activity than activated carbon (AC) and LSCO nanoparticles (NPs) (Figure 8D). The authors then assembled nonaqueous Li−air batteries with these LSCO NWs and

DOI: 10.1021/acscatal.5b01667
ACS Catal. 2015, 5, 6370−6385

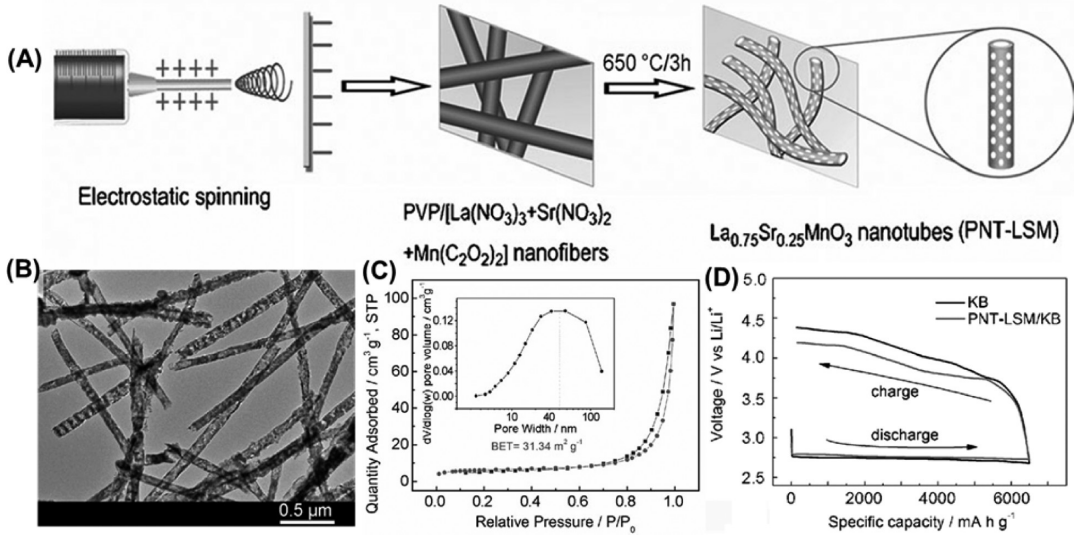

Figure 9. (A) Schematic illustration of the synthesis strategy of the PNT-LSM catalyst. (B) Field-emission scanning electron microscopy image of PNT-LSM. (C) Nitrogen adsorption−desorption isotherms and pore size distribution (inset) of PNT-LSM. (D) First charge−discharge curves of Li−O_2 cells with PNT/ketjenbalck (KB) and KB electrodes at a current density of 0.025 mA cm^{-2}. Reprinted with permission from ref 84. Copyright 2013 Wiley.

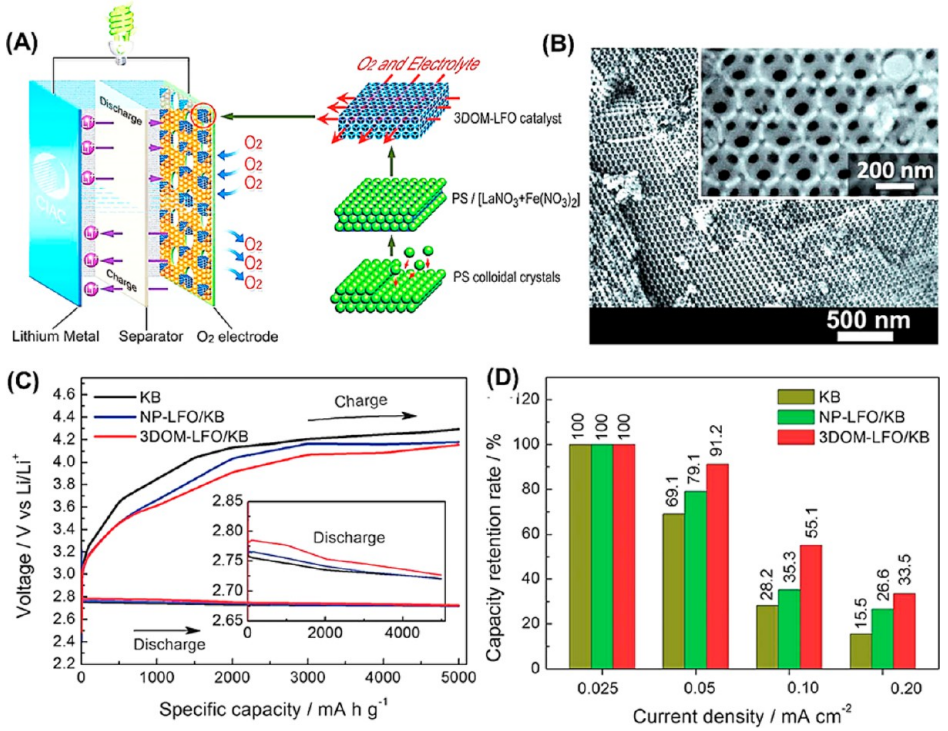

Figure 10. (A) Schematic illustration for preparation of 3DOM-LFO catalyst and structure of the rechargeable Li−O_2 battery. (B) FESEM images of 3DOM-LFO after calcination (inset: magnified FESEM image). (C) Charge−discharge curves of Li−O_2 cells with KB, NP-LFO/KB, and 3DOM-LFO/KB electrodes at a current density of 0.025 mA cm^{-2}. (D) Capacity retention of Li−O_2 cells with KB, NP-LFO/KB and 3DOM-LFO/KB electrodes. Reprinted with permission from ref 87. Copyright 2014 Royal Society of Chemistry.

demonstrated a capacity of over 11 000 mAh g^{-1}. The high performance for the Li−air battery based on the LSCO NWs was attributed to the high specific surface area and the mesoporous structure, which facilitated oxygen transfer during the reaction and at the same time accommodated the decomposed electrolyte and reaction products (Li_2O_2/Li_2O).

Electrospinning was reported to be an effective and scalable approach to producing porous perovskite oxides (Figure 9A).[84] Specifically, this fabrication process included electrostatic spinning to draw the nanofibers of the La-, Sr- and Mn-precursors followed by 650 °C annealing (Figure 9A). The prepared $La_{0.75}Sr_{0.25}MnO_3$ (LSM) demonstrated a porous tubular structure (Figure 9B). The porous LSM nanotubes (PNT-LSM) prepared by this method had a specific surface area of 31.34 m^2 g^{-1} and a pore size ranging from 10 to 30 nm (Figure 9C). This porous structure exhibited a synergistic effect in enhancing Li−O_2 efficiency by reducing both the charge and discharge overpotentials (Figure 9D).

DOI: 10.1021/acscatal.5b01667
ACS Catal. 2015, 5, 6370−6385

The future design of perovskite oxides as electrocatalysts for both ORR and OER will depend on the rational control and tailoring of three-dimensional (3D), high-surface-area architectures. As a replacement for the current dense, compact oxide form, this 3D structure may be enabled by the rational design to further enhance electron and oxygen transfer and preferentially stabilize specific oxygenated intermediates to boost catalysis.[85,86] Recently, Zhang et al. reported a facile strategy for preparing honeycomb-like 3D ordered macroporous $LaFeO_3$ (3DOM-LFO) via polystyrene sphere (PS) template mediating and successfully employed this structure in the O_2 electrode of the Li−O_2 cell.[87] As shown in Figure 10A (right), the monodisperse PS spheres were close-packed into colloidal crystals to form a template by centrifugation and solvent evaporation during drying. The template was then soaked with La- and Fe- metal precursors (metal nitrate). Calcination at high temperature in air removed the template and led to the formation of the 3DOM-LFO. The electrochemical measurement was performed in a coin cell with a lithium foil anode, a separator, and an O_2 electrode containing the prepared 3DOM-LFO, as shown in Figure 10A (left). The well-ordered honeycomb-like pore structure was observed by field-emission scanning electron microscopy (FESEM) (Figure 10B). The interconnected, highly ordered 3DOM structure originated from the close-packed PS template and provided sufficient active sites and surface area to facilitate oxygen and electrolyte diffusion. The round-trip efficiency, associated with the ORR and OER overpotentials, was enhanced by the incorporation of 3DOM-LFO (Figure 10C). More importantly, the capacity retention capability was largely improved with 3DOM-LFO under different current densities (Figure 10D). The enhanced performance was a result of the synergistic effect of the active sites and the porous structure in the 3DOM-LFO. The unique, highly ordered structure of 3DOM-LFO led to the favorable transportation of oxygen and electrolyte inside the electrode.

4. LA-BASED PEROVSKITE OXIDES FOR HETEROGENEOUS CATALYSIS

La-based perovskite oxides are currently at the heart of many energy-related applications. Beyond electrochemical applications, the excellent redox and oxygen mobility properties, as well as the surface acid−base character and good thermal stability, make La-based perovskite oxides verstaile catalysts for heterogeneous reactions. The redox performance of $LaBO_3$ perovskites is mainly controlled by the B-site transition metal element properties, and the role of the rare-earth ions in the A site is secondary.[88,89] For instance, Ma and co-workers studied the reducibility of rare-earth cobaltite by H_2-TPR (temperature-programmed reduction) experiments.[90] It seems that all of the $LnCoO_3$ compounds (Ln = La, Pr, Nd, Sm, Eu, Gd, Tb, Dy) present two reduction peaks (i.e., ∼400 and ∼625 °C), which can be assigned to the $Co^{3+} \rightarrow Co^{2+}$ and $Co^{2+} \rightarrow Co^0$ reduction, respectively.[91] The oxygen mobility in La-based perovskites is generally studied by temperature-programmed desorption (TPD) experiments and isotopic oxygen exchange analysis. It is well-known that La-based perovskites can adsorb a large amount of oxygen species, both on the surface and in the bulk, and desorb two types of oxygen (α-O and β-O).[54,92] The α-O is usually ascribed to oxygen species weakly bound to the surface of the perovskite, which can be observed in the low-temperature desorption peak (<500 °C). The high temperature and sharp peak in O_2-TPD is the result of β-O released mainly from the bulk of the La-based perovskite.

Among the parameters affecting the catalytic activity of La-based perovskite catalysts, the characteristics of the textural property appear to be critical, because they usually determine the active sites accessible for reactants. A traditional method of synthesizing the desired perovskites is calcination of the starting oxide powders through solid-state diffusion. This ceramic method usually requires a high reaction temperature (e.g., >1000 °C) and leads to products with low specific surface areas of 1−2 $m^2\ g^{-1}$. One of the primary goals, which has resulted in tremendous progress in perovskite-based heterogeneous catalysis, is to improve the corresponding specific surface areas of perovskite oxides. Indeed, a number of efficient synthesis routes, such as solution-based processes,[93−96] explosion processes,[97] and mechanochemical strategies,[34] have already been developed toward the optimization of specific surface areas for perovskites. Among them, reactive grinding synthesis is a direct and scalable process. For instance, ball grinding of Mn_2O_3 and La_2O_3 in a zirconia vial containing zirconia balls for 30−120 min can lead to the formation of a $LaMnO_3$ sample with a specific surface area of 9.8 $m^2\ g^{-1}$.[98−100] The citrate sol−gel process is another frequently investigated method for the synthesis of porous La-based perovskites.[101] Initially, citric acid allows the formation of amorphous metal organates with a wide flexibility of composition. Further thermal decomposition of these organates leads to mixed oxides or solid solutions with high homogeneity. In addition, the formation of citrate complexes enables the metal cations to stay well dispersed in the matrix and thus results in the ready formation of perovskite-type oxides, as evidenced by the lower calcination temperature (e.g., 550−650 °C) compared with the acetate process for perovskite phase formation (e.g., 850 °C).[102−105] The specific surface areas of La-based perovskites prepared via this method can reach ∼30 $m^2\ g^{-1}$ under optimized conditions.

4.1. Mesoporous La-Based Perovskite Oxides. Mesoporous materials are entering what can be described as a new golden age in which many novel strategies are emerging because of the revolution in nanoscience.[106,107] Mesoporous structures with many unique characteristics can greatly benefit the inherent performance of solid materials.[108−110] To date, mesoporous La-based perovskites have typically been synthesized by nanocasting hard templates (e.g., mesoporous silicas). The starting precursors are infiltrated inside nanospaces confined by the empty structures (i.e., pore channels) of a hard template. After calcination at high temperature for the formation of perovskite/hard template nanocomposites, the template (e.g., silica) is selectively removed (e.g., by NaOH wash), and the perovskite oxide is obtained. It is ideal if the hard template used has interconnected pore channels; in that case, the perovskites can be expected to form an inverse replica of that template. In the following section, we summarize recent efforts in the synthesis and application of mesoporous La-based perovskite oxides for heterogeneous catalysis. Only a few representative examples will be discussed in detail, as an exhaustive presentation of all the available processes is impossible.

4.1.1. Mesoporous La-Based Perovskite Oxides via Ionic Liquid-Mediated Self Assembly. The emission of CO into the atmosphere is mainly caused by incomplete combustion in automobile engines.[111] The presence of even a small quantity of CO can have a detrimental effect on human health; therefore, it

DOI: 10.1021/acscatal.5b01667
ACS Catal. 2015, 5, 6370−6385

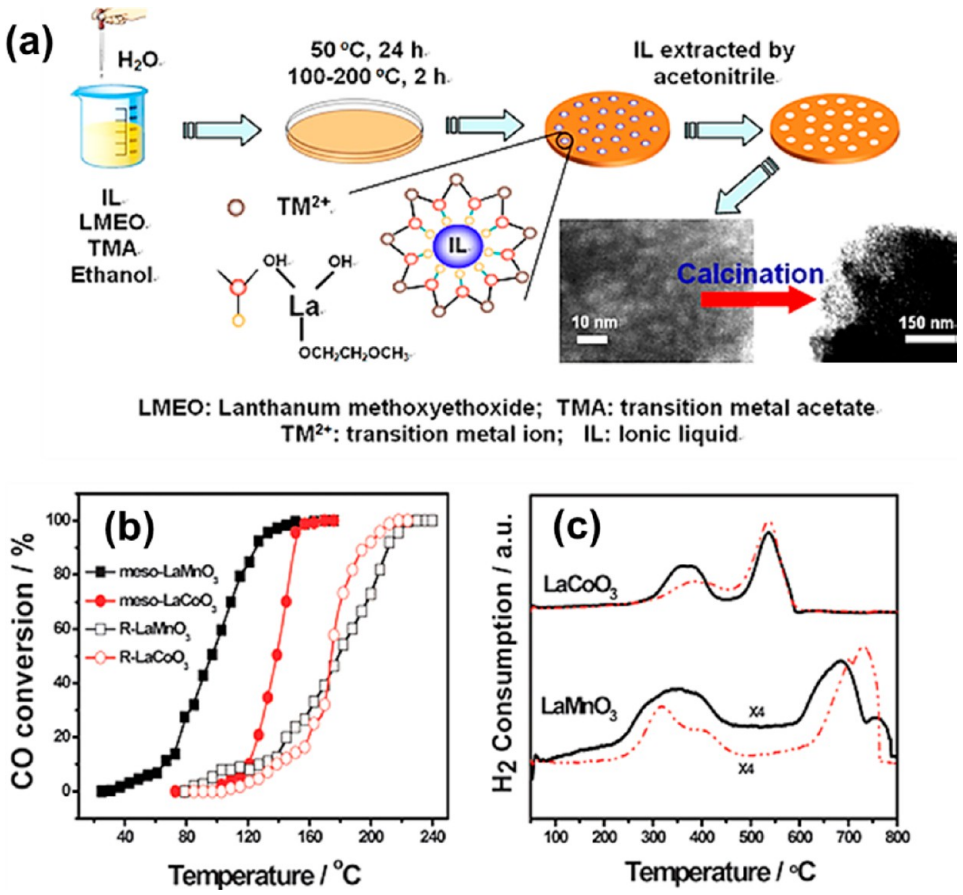

Figure 11. (a) Synthesis process of mesoporous lanthanum transition metal perovskite oxides by ionic liquid. (b) Light-off curves for CO oxidation on meso and referenced $LaMnO_3$ and $LaCoO_3$ (GHSV = 20 000 mL (h gcat)$^{-1}$). Reference samples were prepared by the citrate method. (c) H_2-TPR curves of meso-$LaMnO_3$ and meso-$LaCoO_3$ (black full lines) and R-$LaMnO_3$ and R-$LaCoO_3$ (red dotted lines). Reprinted with permission from ref 116. Copyright 2015 Royal Society of Chemistry.

is urgent to develop efficient catalytic processes to constrain CO emissions. Historically, various types of heterogeneous catalysts have been prepared and used for CO oxidation.[112] For example, platinum-based catalysts show high activity in the oxidation of CO and enable those processes at low temperatures (<473 K).[113] However, issues such as high cost, scarcity, sensitivity to sulfur poisoning, and inferior thermal stability at higher temperatures remain as obstacles for the widespread exploitation of platinum catalysts.[114] $LaMnO_3$ and $LaCoO_3$ have been found to be very active for CO oxidation, and they have the potential to replace noble metal catalysts.[115] Furthermore, partial substitution of Mn or Co can optimize the catalytic activity and material stability.

Nowadays, the materials community is still pursuing soft-templating routes for the synthesis of mesoporous La-based perovskites. Recently, Lu, Dai, and co-workers developed an ionic liquid (IL)-mediated self-assembly strategy to mesoporous La-transition-metal perovskites.[116] It is attractive that the IL additives in the process are recyclable and reusable. This process includes the controlled hydrolysis of La and Mn precursors around large BmimTf2N clusters, the formation of oxo/IL composites under solvent-evaporation-induced self-assembly, the extraction of ILs by washing in ethanol, and further calcination (Figure 11a). Mesoporous $LaMnO_3$ and $LaCoO_3$ demonstrate high activity for CO oxidation compared with reference samples produced by the citrate sol−gel method (Figure 11b). Meso-$LaMnO_3$ enabled 100% CO conversion at 130 °C, and the catalytic activity was stable at 140 °C (100% conversion for CO) for at least 30 h. The H_2-TPR measurements also showed a lower reduction temperature and a higher H_2-consuming amount of meosporous $LaMnO_3$ (Figure 11c). It appears that the unique meso-structures already benefit the catalytic performance of $LaMnO_3$.

4.1.2. Mesoporous La-Based Perovskite Oxides by Hard Templating Strategies. Methane combustion is an important process in natural gas combustion.[117] La-based perovskites have been treated as a class of potential candidates for this reaction, especially considering their high-temperature stability.[118,119] Toward that end, the Lu group reported the synthesis of an ordered mesoporous $LaCoO_3$ perovskite with high surface area via a nanocasting strategy that used ordered mesoporous cubic vinyl silica as the template (Figure 12).[120] The $LaCoO_3$ perovskite with a 3D ordered mesostructure had a high BET surface area of 96.7 m^2 g^{-1} (Figure 12a−c). It showed much higher activity in complete methane oxidation than that of the bulk $LaCoO_3$ perovskite prepared using a conventional citrate method. The light-off temperature (T10, defined as 10% conversion of methane) and the half-conversion temperature (T50) were 335 and 470 °C, respectively (Figure 12d). Both H_2-TPR and X-ray photoelectron spectroscopy techniques showed that a large number of active sites were exposed in the high-surface-area $LaCoO_3$ sample, resulting in a higher catalytic activity. The surface area of the $LaCoO_3$ sample decreased to

DOI: 10.1021/acscatal.5b01667
ACS Catal. 2015, 5, 6370−6385

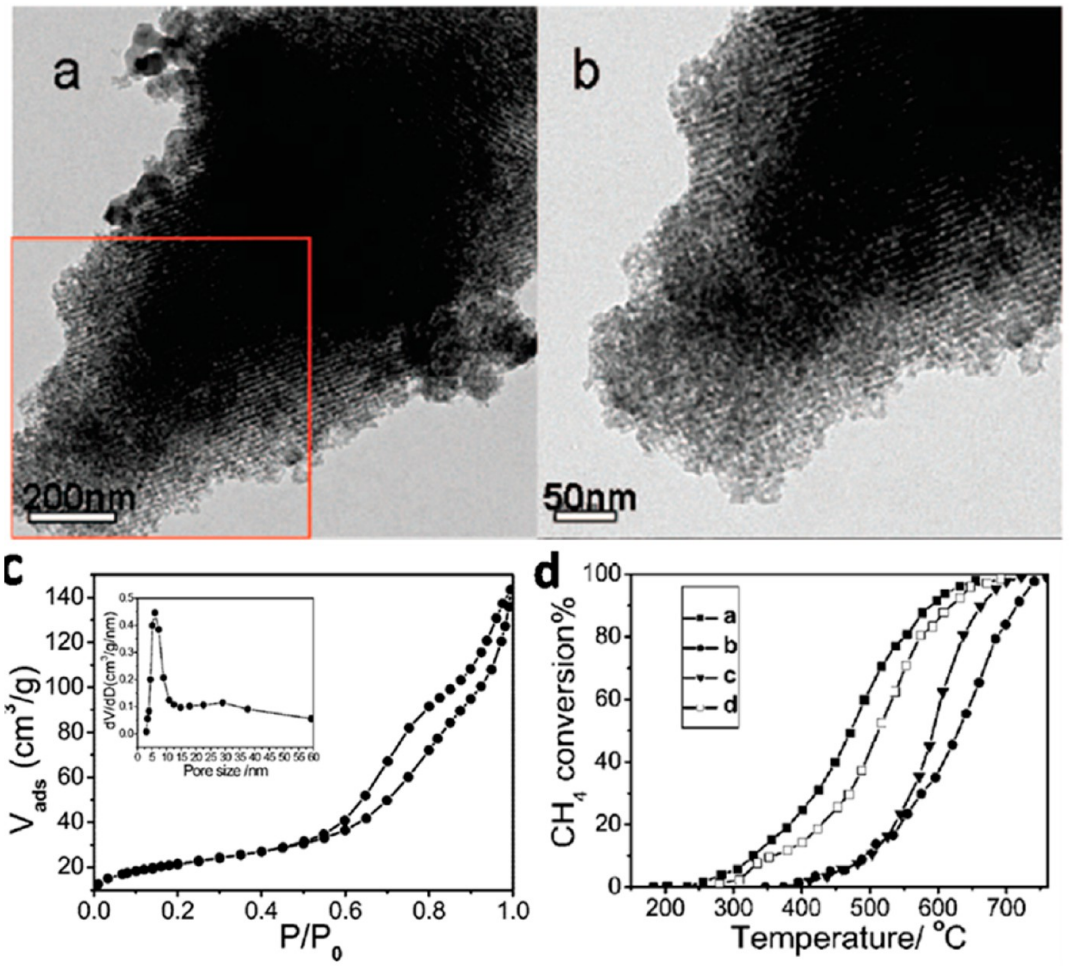

Figure 12. (a) and (b) Transmission electron microscopy image of $LaCoO_3$ sample. (c) N_2 sorption isothermal of $LaCoO_3$ at 77 K. (d) Temperature dependence of methane combustion on different catalysts: (a) mesoporous $LaCoO_3$ after removal of silica, (b) mesoporous $LaCoO_3$/silica hybrid material, (c) conventional $LaCoO_3$, and (d) used mesoporous $LaCoO_3$ catalyst.[120]

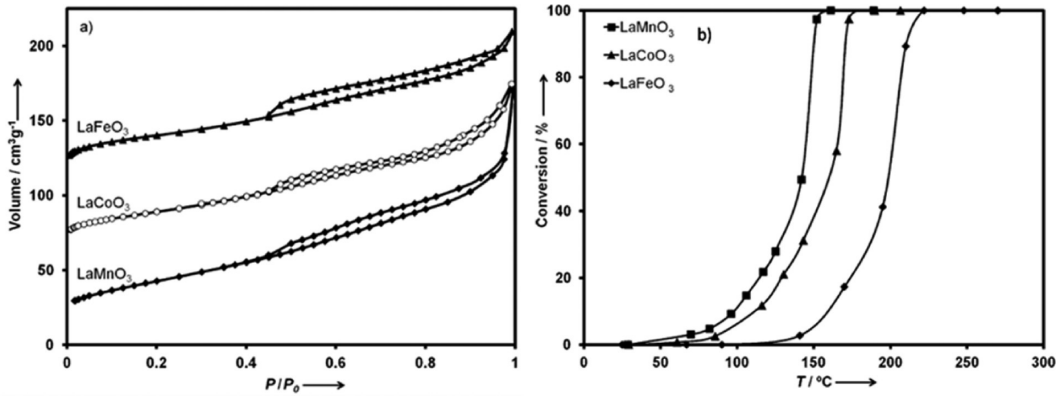

Figure 13. (a) N_2 sorption isotherm of nanocast perovskite oxides synthesized by the replication of ordered mesoporous KIT-6 silica. The isotherms of $LaCoO_3$ and $LaFeO_3$ are plotted with an offset of 60 and 110 cm^3 g^{-1}, respectively, for clarity. (b) Methanol conversion profiles as a function of temperature over $LaMnO_3$, $LaCoO_3$, and $LaFeO_3$ perovskites. Reprinted with permission from ref 121. Copyright 2012 Wiley.

69.5 m^2 g^{-1} after the first run, possibly due to the restructuring of the mesoporous perovskites.

Using the nanocasting method, Nair et al. prepared three mesoporous perovskite oxides by the replication of ordered mesoporous KIT-6 silica (Figure 13).[121] The resulting $LaBO_3$ oxides (B = Mn, Co, Fe) showed very high BET-specific surface area (110−155 m^2 g^{-1}), although this process did not exactly replicate the KIT-6 structures and residual silica or silicates remained in the matrix (containing 3−10% silicon according to atomic absorption analysis). In the oxidation of methanol, the nanocast $LaMnO_3$ clearly exhibited higher conversion efficiency than the sample synthesized by a conventional citrate process. A decrease in the surface area of the $LaMnO_3$ from 155 to 140 m^2 g^{-1} occurred during the methanol oxidation run, in

DOI: 10.1021/acscatal.5b01667
ACS Catal. 2015, 5, 6370−6385

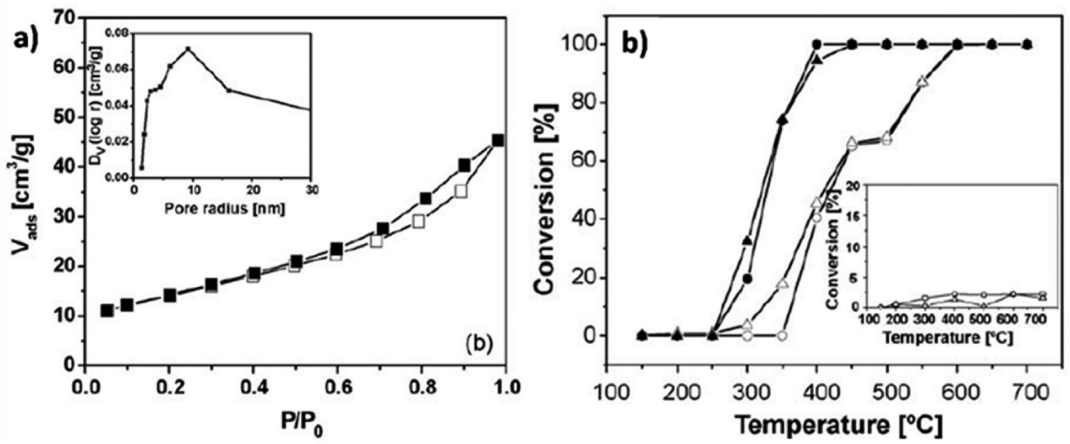

Figure 14. (a) N_2 sorption isotherm curve of nanocast $LaMnO_3$ sample. (b) Temperature profiles for the conversion of NO to N_2 (○, ●) and CO to CO_2 (△, ▲) on uncast $LaFeO_3$ (○, △) and nanocast $LaFeO_3$ (●, ▲). Inset: conversion of NO to N_2 (○) and CO to CO_2 (△) without any catalyst. Reprinted with permission from ref 123. Copyright 2009 Elsevier B.V.

agreement with the observation by the Lu group. It is reasonable that restructuring of nanocast perovskite would occur during the catalytic process. The Kaliaguine group observed a similar result, that the surface area (170 m^2 g^{-1}) of mesoporous nanocast $LaMnO_3$ material decreased to 45 m^2 g^{-1} after thermal treatment at 550 °C for 6 h.[122]

Porous carbon is another type of matrix used for directing porosity into perovskite oxides. For example, high-specific-surface-area $LaFeCoO_3$ perovskites were synthesized by nanocasting in the presence of a micro-/mesoporous carbon mold, which was replicated from a silica Aerosil 200 (Figure 14).[123] The $LaFeO_3$ perovskite sample showed a specific surface area of 49.3 m^2 g^{-1}, lower than the corresponding values for perovskites formed by nanocasting from silica. Under calcination at 800 °C in air, the transformation of inorganic precursors to oxides occurred simultaneously with the removal of the carbon by oxidation, which could lead to the growth or sintering of formed perovskite nanoparticles. Therefore, the confinement effect cannot be completely preserved. During the reduction of NO with CO, the nanocast $LaFeO_3$ perovskite afforded much higher activity than the uncast $LaFeO_3$. For example, the nanocast $LaFeO_3$ perovskite achieved 100% conversions of NO or CO at 400 °C, lower than the value (580 °C) required by the uncast $LaFeO_3$ catalyst. It is thought that the observed higher activity of the nanocast material must be the result of a higher number of accessible active sites induced by its higher specific surface area.

4.2. Supported La-Based Perovskite Oxides. As we dissussed in previous sections, one major limitation of perovskite oxides as efficient heterogeneous catalysts is their low surface area. The main drawback associated with perovskite-oxide nanoparticles is their unfavorable tendency to sinter. At this point, the introduction of a large surface area and thermally stable supports may benefit the exposure of active sites in perovskites. Several problems arise when designing perovskite/support hybrid catalysts: whether the perovskite structure preserves after introducing a support and how to attain a uniform dispersion of perovskite oxides onto supports. Another issue is the decreased weight ratio of active perovskite phases because in most cases support materials are catalytically inactive.

One general method to support La-based perovskites involves the synthesis of porous matrixes and coating perovskite phases on the supports. Alumina- or silica-based supports are generally chemically inert and thus can guarantee the formation of well-defined perovskite phases on the support.[124,125] A number of attempts have been undertaken to support perovskites via the in situ synthesis directly within the pores of aluminia or silica using common metal salts as precursors. However, the catalysts prepared by such a way were found to show rather poor catalytic performance, because nonactive surface aluminate or silicate compounds were formed instead.[126,127] In consideration of the lower temperatures requested for the formation of the perovskite phase, the precursor compunds are usually mixed citrates, oxalates, or cyanide complexes. These precursors were used for the in situ synthesis with mesoporous and high surface area supports (e.g., MCM-41 molecular sieves, SBA-15).[128] Kaliaguine and co-workers supported $LaCoO_3$ on MCM-41, and those composites with 10−50 wt % $LaCoO_3$ inside the MCM-41 mesopores were found to be highly active in complete methane oxidation.[128] Romanovsky et al. studied the physicochemical properties of supported $LaCoO_3$ on MCM-41 as well as its catalytic activity in both complete and partial methanol oxidation. In comparison with bulk $LaCoO_3$, a drastic improvement of the oxidation activity by the supported cobaltate was observed, which has been assigned to a highly disordered oxygen-deficient Co oxide phase stabilized by the La species.[129] The Fan group showed microwave-assisted processing of La−Co citrate precursors into the nanotubular pores of mesoporous SBA-15 silica, resulting in the formation of 5−8.5 nm $LaCoO_3$ perovskite nanocrystals (Figure 15).[130] It seems the growth of $LaCoO_3$ perovskite was confined in the mesopores. The confined $LaCoO_3$ nanocrystals showed superior performance in the complete oxidation of methane, which has been attributed to their high surface area and a much higher density of lattice defects.

Dai, Au, and co-workers developed a one-step strategy for the fabrication of mesoporous y$LaCoO_3$/SBA-15 (y = 10−50 wt %) by in situ hydrothermal treatment of starting materials for SBA-15 and $LaCoO_3$ (Figure 16). Those $LaCoO_3$/SBA-15 held well-defined mesopores with high surface areas (338−567 m^2 g^{-1}), and excellent catalytic performance was observed over the 40$LaCoO_3$/SBA-15 catalyst in the combustion of toluene and ethyl acetate.[131]

DOI: 10.1021/acscatal.5b01667
ACS Catal. 2015, 5, 6370−6385

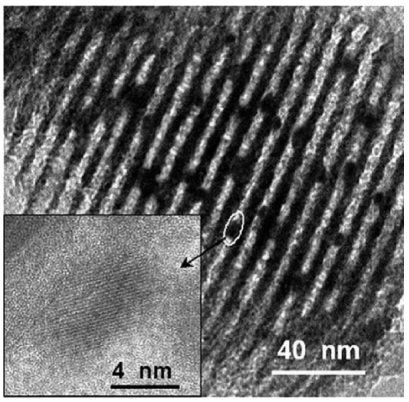

Figure 15. Transmission electron microscopy image (inset shows image of the encircled area at higher magnification) of $LaCoO_3$/SBA-15 composites. Reprinted with permission from ref 130. Copyright 2005 Elsevier B.V.

The alumina or silica supports are often catalytically inactive in heterogeneous oxidations, hence lowering the weight ratio of an active phase in a catalyst, which is not welcome with respect to the catalytic effciency. In this regard, ceria and zirconia may be suitable candidates. For instance, ceria possesses a distinctive feature of oxygen-storage capacity associated with the formation of oxygen vacancies and the low redox potential between Ce^{3+} and Ce^{4+}. Consequently, ceria and zirconia as suitable supports for La−Co perovskites were investigated with an enhanced catalytic activity in propane combustion, comparing with bulk $LaCoO_3$ or $La_{0.8}Sr_{0.2}CoO_3$.[132] Similarly, both $LaCoO_3$ and $LaFeO_3$ supported on ZrO_2 displayed higher catalytic activities than the corresponding bulk perovskites in the oxidation of CO.[133,134] The $LaCoO_3$ phase was also supported on $Ce_{1-x}Zr_xO_2$ supports by wet impregnation with $La(NO_3)_3$, $Co(NO_3)_2$, and citric acid as precursors. A small particle size and a good stoichiometry control were achieved. During the complete oxidation of benzene and toluene, $LaCoO_3$ dispersed on the surface of ceria−zirconia solid solutions decreased the light-off temperatures and at the same time increased with an order of magnitude the reaction rates in comparison with bulk $LaCoO_3$. The increased surface of active sites and enhanced oxygen mobility are believed to enhance this catalytic oxidation.[135−137]

4.3. Ordered Macroporous La-Based Perovskites. Examples of macroporous structured perovskites and their performance in electrocatalysis were briefly discussed in Section 3. Similarly, considering the mass/fluid transfer in heterogeneous catalysis, macroporous channels are also welcome in heterogeneous catalysts. In the past decade, many efforts have been made toward three-dimensional ordered macroporous (3DOM) materials with pores sizes in the submicrometer range. The 3DOM perovskite-type oxides were typically developed by a sol−gel process: (i) the preparation of a colloidal crystal template by ordering monodisperse spheres [e.g., polystyrene, or poly(methyl methacrylate)] into a close-packed array; (ii) filling in the voids of colloidal crystal by liquid metal alkoxides, which is then solidified under a sol−gel transformation, with the formation of an intermediate composite structure; (iii) the formation of an ordered skeleton by calcination at high temperature and at the same time the template is decomposed. The 3DOM structure by inverse opals were interconnected, and thus, an easy and fast mass transport of large molecule through the network and rapid diffuse to active site could be expected.

Common salts of these metals are usually not suitable as metal precursors, because these salts would melt before the templates decompose, and then the 3DOM structure collapses, except a special case with metal nitrates. Liu et al. prepared ordered macroporous $Sr_{0.5}Sm_{0.5}CoO_3$ using monodispersed polystyrene spheres as templates and metal nitrates as precursors.[138] The key consideration in the synthesis of the porous perovskite is to prepare a precursor solution that easily infiltrated the interstitial voids in the PMMA/PS colloids by capillary forces. The selection of suitable metal precursors is an important factor for the successful replica of the colloidal template. Hur and co-workers prepared the metal alkoxide solution by mixing metal acetates and 2-methoxyethanol in HNO_3 and used these in situ formed precursors to infiltrate the PMMA template. Finally, 3DOM $La_{0.7}Ca_{0.3}MnO_3$ was obtained, and it is one of the pioneering works in this topic.[139,140] Ueda et al. described a facile preparation of 3DOM perovskite ($La_{1-x}Sr_xFeO_3$, x = 0−0.4), from an ethylene glycol solution of metal nitrate salts. The precusors turned into a mixed metal glyoxylate salt following an in situ nitrate oxidation at a relatively low temperature before the removal of the colloidal template.[141]

Recently, the Dai group at Beijing University of Technology developed a number of 3DOM-structured perovskites with high surface areas by surfactant-assisted PMMA templating approaches, and some of them have been shown to be very active in catalytic oxidation.[142−145] For instance, Dai and co-workers[146] showed a poly(ethylene glycol) (PEG)400- and triblock copolymer (Pluronic P123)-promoted PMMA templating strategy, leading to $LaMnO_3$ with high-quality 3DOM structures, nanovoid skeletons, and high surface areas (37−39 m^2 g^{-1}) (Figure 17). The porous $LaMnO_3$ samples were

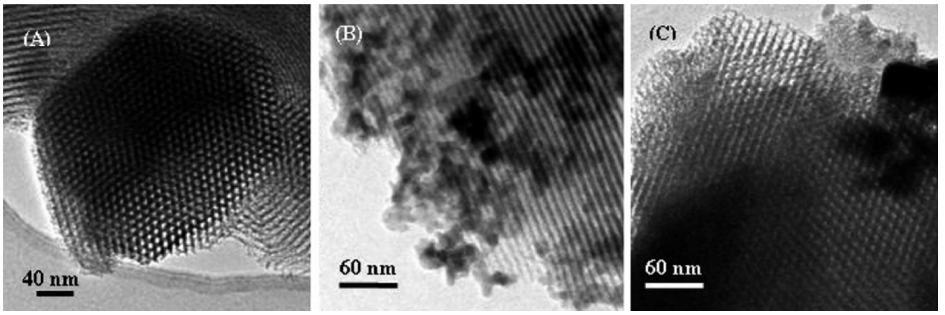

Figure 16. TEM images of as-prepared (A) 35$LaCoO_3$/SBA-15, (B) 35$LaCoO_3$/SBA-15_imp (prepared by impregnation method), and (C) 50$LaCoO_3$/SBA-15 catalysts. Reprinted with permission from ref 131. Copyright 2009 Elsevier B.V.

DOI: 10.1021/acscatal.5b01667
ACS Catal. 2015, 5, 6370−6385

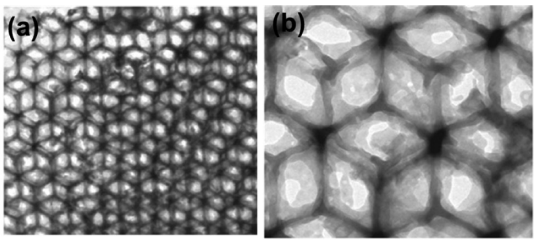

Figure 17. HRTEM images $LaMnO_3$−PEG. Reprinted with permission from ref 146. Copyright 2012 Elsevier B.V.

superior to the bulk counterpart in the catalytic combustion of toluene, with the nanovoid-containing 3DOM-structured $LaMnO_3$ catalyst performing the best.[146] Zhao et al. also reported the facile synthesis of 3DOM $La_{1-x}K_xCoO_3$ (x = 0−0.3) perovskites by the carboxy-modified colloidal crystal templating method. The sp^2-hybridized carbon atoms of the modified PMMA templates can be converted to the stable amorphous carbon by calcination under an inert atmosphere to prevent the macrostructure from collapsing, whereas the carbon inside can be removed later by calcination in air.[147]

5. SUMMARY

In summary, this article highlights old discoveries and recent developments in La-based perovskite oxides as catalysts for the electrochemical conversion of oxygen (ORR/OER) and heterogeneous reactions (CO/CH_4 oxidation, methanol/NO conversion). The B-site substitution effects on both electrocatalysis and heterogeneous catalysis are discussed in detail with various $LaBO_3$ (B = Fe, Co, Ni, Mn, Cr, etc.) materials and their partial substitutions as examples. The redox behavior of B-site cations is considered to govern oxygen adsorption and transport during catalysis. Specifically, Mn and Co cations on the B sites were very active in catalyzing ORR and increasing oxygen mobility owing to their redox potential near the oxygen reduction potential. Sections 2 and 3 are devoted to recent advances in La-based perovskite oxides for ORR/OER catalysis. The reaction descriptor for both ORR/OER and the possible reaction mechanism on the perovskite oxides is demonstrated to be dependent on the e_g orbital occupancy. With the e_g occupancy number close to unity, the intrinsic ORR and OER activity of La-based perovskite oxides can be optimized. However, the exact reaction mechanism for ORR/OER in La-based perovskite oxides of different compositions and prepared by various methods is not fully understood and needs further study. With an emphasis on La-based perovskite oxides, the partial substitution of other elements (e.g., Sr, Ce) for La and the corresponding influence on crystalline structure, valence state, and catalytic performance are briefly discussed. Section 3 also reviews some most recent studies on La-based perovskite oxides implemented in new energy schemes, such as Li−air batteries and La-based perovskite oxides have been found to demonstrate promising performance. Section 4 mainly reviews traditional and developing fabrication techniques for La-based perovskite oxides and their performance in heterogeneous catalysis.

To date, La-based perovskite oxides prepared by various methods perform inconsistently with respect to one another, making comparisons among different systems extremely difficult. The challenges and future direction with regard to benchmarking La-based perovskite oxide catalysts lie in the pursuit of versatile, universal fabrication methods to achieve high specific surface areas and abundant active sites within the structure. Moreover, several issues need to be addressed in the future to fully reveal the potential of perovskite oxides and employ them as replacements for noble metal catalysts:

(1) The electronic conductivity of La-based perovskite oxides must be substantially improved before they can be viably applied in electrochemical-related energy devices.
(2) Fabrication of La-based perovskite oxides with high surface area should be further pursued. This aim can be realized by developing preparation methods either for porous structured materials or for nanosize particles. Moreover, monodispersed La-based perovskite oxide nanoparticles should be synthesized to provide a deep understanding of the relationship between the parameters of the nanoparticles and their physical and chemical properties.
(3) The 3D structured La-based perovskite oxides may become the most promising candidates for electrochemical and heterogeneous catalysis, as they can provide interconnected channels to maximize the exposure of metal cations to electrons (from the electrode) and ions (from the solution) and to accommodate reactants and intermediates. To this end, the quest for a feasible method of synthesizing 3D La-based perovskite oxides is highly important.

AUTHOR INFORMATION

Corresponding Authors

*E-mail: zhuh@ornl.gov.
*E-mail: dais@ornl.gov.

Notes

The authors declare no competing financial interest.

ACKNOWLEDGMENTS

P. Z. and S. D. were supported by the U.S. Department of Energy, Office of Science, Chemical Sciences, Geosciences and Biosciences Division. H. Z. acknowledges the Liane B. Russell Fellowship at Oak Ridge National Laboratory, managed by UT-Battelle, LLC, for the US Department of Energy.

REFERENCES

(1) Peña, M. A.; Fierro, J. L. G. *Chem. Rev.* **2001**, *101*, 1981−2017.
(2) Schaak, R. E.; Mallouk, T. E. *Chem. Mater.* **2002**, *14*, 1455−1471.
(3) Royer, S.; Duprez, D.; Can, F.; Courtois, X.; Batiot-Dupeyrat, C.; Laassiri, S.; Alamdari, H. *Chem. Rev.* **2014**, *114*, 10292−10368.
(4) Zhu, J.; Li, H.; Zhong, L.; Xiao, P.; Xu, X.; Yang, X.; Zhao, Z.; Li, J. *ACS Catal.* **2014**, *4*, 2917−2940.
(5) Ngamou, P. H. T.; Bahlawane, N. *Chem. Mater.* **2010**, *22*, 4158−4165.
(6) Natile, M. M.; Ugel, E.; Maccato, C.; Glisenti, A. *Appl. Catal., B* **2007**, *72*, 351−362.
(7) Kim, C. H.; Qi, G.; Dahlberg, K.; Li, W. *Science* **2010**, *327*, 1624−1626.
(8) Nitadori, T.; Misono, M. *J. Catal.* **1985**, *93*, 459−466.
(9) García de la Cruz, R. M.; Falcón, H.; Peña, M. A.; Fierro, J. L. G. *Appl. Catal., B* **2001**, *33*, 45−55.
(10) Nitadori, T.; Kurihara, S.; Misono, M. *J. Catal.* **1986**, *98*, 221−228.
(11) Mefford, J. T.; Hardin, W. G.; Dai, S.; Johnston, K. P.; Stevenson, K. J. *Nat. Mater.* **2014**, *13*, 726−732.
(12) Mueller, D. N.; Machala, M. L.; Bluhm, H.; Chueh, W. C. *Nat. Commun.* **2015**, *6*, 6097.
(13) Bockris, J. O. M.; Otagawa, T.; Young, V. *J. Electroanal. Chem. Interfacial Electrochem.* **1983**, *150*, 633−643.

DOI: 10.1021/acscatal.5b01667
ACS Catal. 2015, 5, 6370−6385

(14) Bockris, J. O. M.; Otagawa, T. *J. Electrochem. Soc.* **1984**, *131*, 290−302.
(15) Vojvodic, A.; Nørskov, J. K. *Science* **2011**, *334*, 1355−1356.
(16) Hyodo, T.; Hayashi, M.; Miura, N.; Yamazoe, N. *J. Electrochem. Soc.* **1996**, *143*, L266−L267.
(17) Guo, S.; Zhang, S.; Sun, S. *Angew. Chem., Int. Ed.* **2013**, *52*, 8526−8544.
(18) Zhu, H.; Zhang, S.; Guo, S.; Su, S.; Sun, S. *J. Am. Chem. Soc.* **2013**, *135*, 7130−7133.
(19) Zhang, S.; Hao, Y.; Su, D.; Doan-Nguyen, V. V. T.; Wu, Y.; Li, J.; Sun, S.; Murray, C. B. *J. Am. Chem. Soc.* **2014**, *136*, 15921−15924.
(20) Zhu, H.; Zhang, S.; Su, D.; Jiang, G.; Sun, S. *Small* **2015**, *11*, 3545−3549.
(21) Meadowcroft, D. B. *Nature* **1970**, *226*, 847−848.
(22) Zhu, H.; Zhang, S.; Huang, Y. X.; Wu, L.; Sun, S. *Nano Lett.* **2013**, *13*, 2947−2951.
(23) Sunarso, J.; Torriero, A. A. J.; Zhou, W.; Howlett, P. C.; Forsyth, M. *J. Phys. Chem. C* **2012**, *116*, 5827−5834.
(24) Suntivich, J.; Gasteiger, H. A.; Yabuuchi, N.; Shao-Horn, Y. *J. Electrochem. Soc.* **2010**, *157*, B1263−B1268.
(25) Adler, S. B. *Solid State Ionics* **1998**, *111*, 125−134.
(26) Adler, S. B. *J. Electrochem. Soc.* **1996**, *143*, 3554−3564.
(27) Adler, S. B. *Chem. Rev.* **2004**, *104*, 4791−4844.
(28) Ohno, Y.; Nagata, S.; Sato, H. *Solid State Ionics* **1981**, *3*−*4*, 439−442.
(29) Poux, T.; Napolskiy, F. S.; Dintzer, T.; Kéranguéven, G.; Istomin, S. Y.; Tsirlina, G. A.; Antipov, E. V.; Savinova, E. R. *Catal. Today* **2012**, *189*, 83−92.
(30) Hu, J.; Wang, L.; Shi, L.; Huang, H. *J. Power Sources* **2014**, *269*, 144−151.
(31) Li, X.; Qu, W.; Zhang, J.; Wang, H. *J. Electrochem. Soc.* **2011**, *158*, A597−A604.
(32) Poux, T.; Bonnefont, A.; Kéranguéven, G.; Tsirlina, G. A.; Savinova, E. R. *ChemPhysChem* **2014**, *15*, 2108−2120.
(33) Jörissen, J. *J. Power Sources* **2006**, *155*, 23−32.
(34) Kaliaguine, S.; Van Neste, A. Process for synthesizing metal oxides and metal oxides having a perovskite or perovskite-like crystal structure. U.S. Patent 6,770,256, 2004.
(35) Kaliaguine, S.; Van Neste, A. Process for synthesizing perovskites using high energy milling. U.S. Patent 6,017,504, 2000.
(36) Lamminen, J. K.; Kivisaari, J.; Lampinen, M. J.; Viitanen, M.; Vuorisalo, J. *J. Electrochem. Soc.* **1991**, *138*, 905−908.
(37) Chen, Z.; Yu, A. P.; Higgins, D.; Li, H.; Wang, H. J.; Chen, Z. *Nano Lett.* **2012**, *12*, 1946−1952.
(38) Hardin, W. G.; Slanac, D. A.; Wang, X.; Dai, S.; Johnston, K. P.; Stevenson, K. J. *J. Phys. Chem. Lett.* **2013**, *4*, 1254−1259.
(39) Suntivich, J.; Gasteiger, H. A.; Yabuuchi, N.; Nakanishi, H.; Goodenough, J. B.; Shao-Horn, Y. *Nat. Chem.* **2011**, *3*, 546−550.
(40) Tejuca, L. G.; Fierro, J. L. G.; Tascon, J. M. D. *Adv. Catal.* **1989**, *36*, 237−328.
(41) Dowden, D. A. *Catal. Rev.: Sci. Eng.* **1971**, *5*, 1−32.
(42) Sabatier, P. *Ber. Dtsch. Chem. Ges.* **1911**, *44*, 1984−2001.
(43) Stamenkovic, V. R.; Mun, B. S.; Arenz, M.; Mayrhofer, K. J. J.; Lucas, C. A.; Wang, G.; Ross, P. N.; Markovic, N. M. *Nat. Mater.* **2007**, *6*, 241−247.
(44) Zhang, D.; Song, Y.; Du, Z.; Wang, L.; Li, Y.; Goodenough, J. B. *J. Mater. Chem. A* **2015**, *3*, 9421−9426.
(45) Ono, K.; Kinumoto, T.; Tsumura, T.; Toyoda, M. *ECS Trans.* **2015**, *64*, 29−39.
(46) Stoerzinger, K. A.; Risch, M.; Suntivich, J.; Lu, W. M.; Zhou, J.; Biegalski, M. D.; Christen, H. M.; Ariando; Venkatesan, T.; Shao-Horn, Y. *Energy Environ. Sci.* **2013**, *6*, 1582−1588.
(47) Sakthivel, M.; Bhandari, S.; Drillet, J. F. *ECS Electrochem. Lett.* **2015**, *4*, A56−A58.
(48) Yuasa, M.; Shimanoe, K.; Teraoka, Y.; Yamazoe, N. *Electrochem. Solid-State Lett.* **2011**, *14*, A67−A69.
(49) Yuasa, M.; Yamazoe, N.; Shimanoe, K. *J. Electrochem. Soc.* **2011**, *158*, A411−A416.
(50) Zhu, Y.; Zhou, W.; Chen, Y.; Yu, J.; Xu, X.; Su, C.; Tade, M. O.; Shao, Z. *Chem. Mater.* **2015**, *27*, 3048−3054.
(51) Ferri, D.; Forni, L. *Appl. Catal., B* **1998**, *16*, 119−126.
(52) Takeda, Y.; Kanno, R.; Noda, M.; Yamamoto, O. *Bull. Inst. Chem. Res.* **1986**, *64*, 157−160.
(53) Crumlin, E. J.; Ahn, S. J.; Lee, D.; Mutoro, E.; Biegalski, M. D.; Christen, H. M.; Shao-Horn, Y. *J. Electrochem. Soc.* **2012**, *159*, F219−F225.
(54) Ponce, S.; Peña, M. A.; Fierro, J. L. G. *Appl. Catal., B* **2000**, *24*, 193−205.
(55) Suresh, K.; Panchapagesan, T. S.; Patil, K. C. *Solid State Ionics* **1999**, *126*, 299−305.
(56) Yuan, X. Z.; Li, X.; Qu, W.; Ivey, D. G.; Wang, H. *ECS Trans.* **2011**, *35*, 11−20.
(57) Tulloch, J.; Donne, S. W. *J. Power Sources* **2009**, *188*, 359−366.
(58) Stoerzinger, K. A.; Lu, W.; Li, C.; Ariando; Venkatesan, T.; Shao-Horn, Y. *J. Phys. Chem. Lett.* **2015**, *6*, 1435−1440.
(59) Zhang, S.; Guo, S.; Zhu, H.; Su, D.; Sun, S. *J. Am. Chem. Soc.* **2012**, *134*, 5060−5063.
(60) Zhang, S.; Zhang, X.; Jiang, G.; Zhu, H.; Guo, S.; Su, D.; Lu, G.; Sun, S. *J. Am. Chem. Soc.* **2014**, *136*, 7734−7739.
(61) Li, Q.; Wu, L.; Wu, G.; Su, D.; Lv, H.; Zhang, S.; Zhu, W.; Casimir, A.; Zhu, H.; Mendoza-Garcia, A.; Sun, S. *Nano Lett.* **2015**, *15*, 2468−2473.
(62) Zhou, W.; Sunarso, J. *J. Phys. Chem. Lett.* **2013**, *4*, 2982−2988.
(63) Wang, G.; Xu, T.; Wen, S.; Pan, M. *Sci. China: Chem.* **2015**, *58*, 871−878.
(64) Kudo, A.; Miseki, Y. *Chem. Soc. Rev.* **2009**, *38*, 253−278.
(65) Shao, Y.; Park, S.; Xiao, J.; Zhang, J. G.; Wang, Y.; Liu, J. *ACS Catal.* **2012**, *2*, 844−857.
(66) Walter, M. G.; Warren, E. L.; McKone, J. R.; Boettcher, S. W.; Mi, X.; Santori, E. A.; Lewis, N. S. *Chem. Rev.* **2010**, *110*, 6446−6473.
(67) Fang, Y. H.; Liu, Z. P. *J. Am. Chem. Soc.* **2010**, *132*, 18214−18222.
(68) Sanchez Casalongue, H. G.; Ng, M. L.; Kaya, S.; Friebel, D.; Ogasawara, H.; Nilsson, A. *Angew. Chem., Int. Ed.* **2014**, *53*, 7169−7172.
(69) Lee, Y.; Suntivich, J.; May, K. J.; Perry, E. E.; Shao-Horn, Y. *J. Phys. Chem. Lett.* **2012**, *3*, 399−404.
(70) Otagawa, T.; Bockris, J. O. M. *J. Electrochem. Soc.* **1982**, *129*, 2391−2392.
(71) Suntivich, J.; May, K. J.; Gasteiger, H. A.; Goodenough, J. B.; Shao-Horn, Y. *Science* **2011**, *334*, 1383−1385.
(72) Rossmeisl, J.; Qu, Z. W.; Zhu, H.; Kroes, G. J.; Nørskov, J. K. *J. Electroanal. Chem.* **2007**, *607*, 83−89.
(73) Man, I. C.; Su, H. Y.; Calle-Vallejo, F.; Hansen, D. A.; Martínez, J. I.; Inoglu, N. G.; Kitchin, J.; Jaramillo, T. F.; Nørskov, K. J.; Rossmeisl, J. *ChemCatChem* **2011**, *3*, 1159−1165.
(74) Malkhandi, S.; Trinh, P.; Manohar, A. K.; Manivannan, A.; Balasubramanian, M.; Surya Prakash, G. K.; Narayanan, S. R. *J. Phys. Chem. C* **2015**, *119*, 8004−8013.
(75) Seo, M. H.; Park, H. W.; Lee, D. U.; Park, M. G.; Chen, Z. *ACS Catal.* **2015**, *5*, 4337−4344.
(76) Cheng, F.; Chen, J. *Chem. Soc. Rev.* **2012**, *41*, 2172−2192.
(77) Christensen, J.; Albertus, P.; Sanchez-Carrera, R. S.; Lohmann, T.; Kozinsky, B.; Liedtke, R.; Ahmed, J.; Kojic, A. *J. Electrochem. Soc.* **2012**, *159*, R1−R30.
(78) Wang, Y. G.; Ren, J. W.; Wang, Y. Q.; Zhang, F. Y.; Liu, X. H.; Guo, Y.; Lu, G. Z. *J. Phys. Chem. C* **2008**, *112*, 15293−15298.
(79) Nair, M. M.; Kleitz, F.; Kaliaguine, S. *ChemCatChem* **2012**, *4*, 387−394.
(80) Fu, Z.; Lin, X.; Huang, T.; Yu, A. *J. Solid State Electrochem.* **2012**, *16*, 1447−1452.
(81) Yang, W.; Salim, J.; Li, S.; Sun, C.; Chen, L.; Goodenough, J. B.; Kim, Y. *J. Mater. Chem.* **2012**, *22*, 18902−18907.
(82) Jung, J. I.; Jeong, H. Y.; Lee, J. S.; Kim, M. G.; Cho, J. *Angew. Chem., Int. Ed.* **2014**, *53*, 4582−4586.
(83) Zhao, Y.; Xu, L.; Mai, L.; Han, C.; An, Q.; Xu, X.; Liu, X.; Zhang, Q. *Proc. Natl. Acad. Sci. U. S. A.* **2012**, *109*, 19569−19574.

DOI: 10.1021/acscatal.5b01667
ACS Catal. 2015, 5, 6370−6385

(84) Xu, J. J.; Xu, D.; Wang, Z. L.; Wang, H. G.; Zhang, L. L.; Zhang, X. B. *Angew. Chem., Int. Ed.* **2013**, *52*, 3887−3890.
(85) Yang, P.; Rizvi, A. H.; Messer, B.; Chmelka, B. F.; Whitesides, G. M.; Stucky, G. D. *Adv. Mater.* **2001**, *13*, 427−431.
(86) Trotochaud, L.; Boettcher, S. W. *Scr. Mater.* **2013**, *74*, 25−32.
(87) Xu, J. J.; Wang, Z. L.; Xu, D.; Meng, F. Z.; Zhang, X. B. *Energy Environ. Sci.* **2014**, *7*, 2213−2219.
(88) Nitadori, T.; Ichiki, T.; Misono, M. *Bull. Chem. Soc. Jpn.* **1988**, *61*, 621−626.
(89) Kremenić, G.; Nieto, J. M. L.; Tascón, J. M. D.; Tejuca, L. G. *J. Chem. Soc., Faraday Trans. 1* **1985**, *81*, 939−949.
(90) Futai, M.; Yonghua, C.; Louhui. *React. Kinet. Catal. Lett.* **1986**, *31*, 47−54.
(91) Crespin, M.; Hall, W. K. *J. Catal.* **1981**, *69*, 359−370.
(92) Kirchnerova, J.; Alifanti, M.; Delmon, B. *Appl. Catal., A* **2002**, *231*, 65−80.
(93) Wachowski, L. *Surf. Coat. Technol.* **1986**, *29*, 303−311.
(94) Taguchi, H.; Yamada, S.; Nagao, M.; Ichikawa, Y.; Tabata, K. *Mater. Res. Bull.* **2002**, *37*, 69−76.
(95) Ng lee, Y.; Lago, R. M.; Fierro, J. L. G.; Gonzalez, J. *Appl. Catal., A* **2001**, *215*, 245−256.
(96) Tejuca, L. G.; Fierro, J. L. G.; Tascon, J. M. D. *Adv. Catal.* **1989**, *36*, 237−328.
(97) Wachowski, L.; Zielinski, S.; Burewicz, A. *Acta. Chim. Acad. Sci. Hung.* **1981**, *106*, 217−225.
(98) Zhang, Q.; Saito, F. *J. Alloys Compd.* **2000**, *297*, 99−103.
(99) Zhang, Q.; Saito, F. *J. Mater. Sci.* **2001**, *36*, 2287−2290.
(100) Zhang, Q.; Lu, J.; Saito, F. *Powder Technol.* **2002**, *122*, 145−149.
(101) Taguchi, H.; Matsuura, S.-I.; Nagao, M.; Choso, T.; Tabata, K. *J. Solid State Chem.* **1997**, *129*, 60−65.
(102) Courty, P.; Ajot, H.; Marcilly, C.; Delmon, B. *Powder Technol.* **1973**, *7*, 21−38.
(103) Zhang, H. M.; Teraoka, Y.; Yamazoe, N. *Chem. Lett.* **1987**, *16*, 665−668.
(104) Taguchi, H.; Yamasaki, S.; Itadani, A.; Yosinaga, M.; Hirota, K. *Catal. Commun.* **2008**, *9*, 1913−1936.
(105) Huizaz-Félix, A. M.; Hernadez, T.; de la Parra, S.; Ibarra, J.; Kharisov, B. *Powder Technol.* **2012**, *229*, 290−293.
(106) Wan, Y.; Shi, Y.; Zhao, D. Y. *Chem. Mater.* **2008**, *20*, 932−945.
(107) Qiao, Z.; Zhang, P. F.; Chai, S.; Chi, M.; Veith, G. M.; Gallego, N. C.; Kidder, M.; Dai, S. *J. Am. Chem. Soc.* **2014**, *136*, 11260−11263.
(108) Poyraz, A. S.; Kuo, C.; Biswas, S.; King'ondu, C. K.; Suib, S. L. *Nat. Commun.* **2013**, *4*, 2952.
(109) Meng, Y.; Song, W.; Huang, H.; Ren, Z.; Chen, S.; Suib, S. L. *J. Am. Chem. Soc.* **2014**, *136*, 11452−11464.
(110) Zhang, P. F.; Zhu, H. Y.; Dai, S. *ChemCatChem* **2015**, *7*, 2788−2805.
(111) Yang, F.; Graciani, J.; Evans, J.; Liu, P.; Hrbek, J.; Sanz, J. F.; Rodriguez, J. A. *J. Am. Chem. Soc.* **2011**, *133*, 3444−3451.
(112) Royer, S.; Duprez, D. *ChemCatChem* **2011**, *3*, 24−65.
(113) Zhu, H.; Wu, Z.; Su, D.; Veith, G. M.; Lu, H.; Zhang, P.; Chai, S.; Dai, S. *J. Am. Chem. Soc.* **2015**, *137*, 10156−10159.
(114) Imanaka, N.; Masui, T.; Imadzu, H.; Yasuda, K. *Chem. Commun.* **2011**, *47*, 11032−11034.
(115) Xiao, P.; Zhu, J. J.; Li, H. L.; Jiang, W.; Wang, T.; Zhu, Y. J.; Zhao, Y. X.; Li, J. L. *ChemCatChem* **2014**, *6*, 1774−1781.
(116) Lu, H. F.; Zhang, P. F.; Qiao, Z.-A.; Zhang, J. S.; Zhu, H. Y.; Chen, J. H.; Chen, Y. F.; Dai, S. *Chem. Commun.* **2015**, *51*, 5910−5913.
(117) Schwartz, W. R.; Ciuparu, D.; Pfefferle, L. D. *J. Phys. Chem. C* **2012**, *116*, 8587−8593.
(118) Wei, X.; Hug, P.; Figi, R.; Trottmann, M.; Weidenkaff, A.; Ferri, D. *Appl. Catal., B* **2010**, *94*, 27−37.
(119) Chen, C.; Li, W.; Cao, C.; Song, W.-G. *J. Mater. Chem.* **2010**, *20*, 6968−6974.
(120) Wang, Y.; Ren, J.; Wang, Y.; Zhang, F.; Liu, X.; Guo, Y.; Lu, G. Z. *J. Phys. Chem. C* **2008**, *112*, 15293−15298.
(121) Nair, M. M.; Kleitz, F.; Kaliaguine, S. *ChemCatChem* **2012**, *4*, 387−394.
(122) Sarshar, Z.; Kleitz, F.; Kaliaguine, S. *Energy Environ. Sci.* **2011**, *4*, 4258−4269.
(123) de Lima, R. K. C.; Batista, M. S.; Wallau, M.; Sanches, E. A.; Mascarenhas, Y. P.; Urquieta-González, E. A. *Appl. Catal., B* **2009**, *90*, 441−450.
(124) Labhsetwar, N. K.; Watanabe, A.; Biniwale, R. B.; Kumar, R.; Mitsuhashi, T. *Appl. Catal., B* **2001**, *33*, 165−173.
(125) Burch, R.; Harris, P. J. F.; Pipe, C. *Appl. Catal., A* **2001**, *210*, 63−73.
(126) Mizuno, N. *Catal. Today* **1990**, *8*, 221−230.
(127) Mizuno, N.; Fujii, H.; Misono, M. *Chem. Lett.* **1986**, *15*, 1333−1336.
(128) Nguyen, S. V.; Szabo, V.; Trong, D. O.; Kaliaguine, S. *Microporous Mesoporous Mater.* **2002**, *54*, 51−61.
(129) Makshina, E. V.; Sirotin, S. V.; van den Berg, M. W. E.; Klementiev, K. V.; Yushchenko, V. V.; Mazo, G. N.; Grünert, W.; Romanovsky, B. V. *Appl. Catal., A* **2006**, *312*, 59−66.
(130) Yi, N.; Cao, Y.; Su, Y.; Dai, W.; He, H.; Fan, K. *J. Catal.* **2005**, *230*, 249−253.
(131) Deng, J.; Zhang, L.; Dai, H.; Au, C. *Appl. Catal., A* **2009**, *352*, 43−49.
(132) Fujii, H.; Mizuno, N.; Misono, M. *Chem. Lett.* **1987**, 2147−2150.
(133) Chand, S.; Sharma, A. K.; Garg, A.; Mishra, I. M. *J. Sci. Ind. Res.* **2000**, *59*, 944−948.
(134) Colonna, S.; De Rossi, S.; Faticanti, M.; Pettiti, I.; Porta, P. *J. Mol. Catal. A: Chem.* **2002**, *187*, 269−276.
(135) Alifanti, M.; Florea, M.; Pârvulescu, V. I. *Appl. Catal., B* **2007**, *70*, 400−405.
(136) Alifanti, M.; Blangenois, N.; Florea, M.; Delmon, B. *Appl. Catal., A* **2005**, *280*, 255−265.
(137) Alifanti, M.; Florea, M.; Somacescu, S.; Pârvulescu, V. I. *Appl. Catal., B* **2005**, *60*, 33−39.
(138) Chen, F.; Xia, C.; Liu, M. *Chem. Lett.* **2001**, *30*, 1032−1033.
(139) Chi, E. O.; Kim, Y. N.; Kim, J. C.; Hur, N. H. *Chem. Mater.* **2003**, *15*, 1929−1931.
(140) Kim, Y. N.; Kim, S. J.; Lee, E. K.; Chi, E. O.; Hur, N. H.; Hong, C. S. *J. Mater. Chem.* **2004**, *14*, 1774−1777.
(141) Sadakane, M.; Asanuma, T.; Kubo, J.; Ueda, W. *Chem. Mater.* **2005**, *17*, 3546−3551.
(142) Ji, K.; Dai, H.; Deng, J.; Song, L.; Gao, B.; Wang, Y.; Li, X. *Appl. Catal., B* **2013**, *129*, 539−548.
(143) Ji, K.; Dai, H.; Deng, J.; Li, X.; Wang, Y.; Gao, B.; Bai, G.; Au, C. T. *Appl. Catal., A* **2012**, *447−448*, 41−48.
(144) Yuan, J.; Dai, H.; Zhang, L.; Deng, J.; Liu, Y.; Zhang, H.; Jiang, H.; He, H. *Catal. Today* **2011**, *175*, 209−215.
(145) Ji, K.; Dai, H.; Deng, J.; Zhang, L.; Wang, F.; Jiang, H.; Au, C. T. *Appl. Catal., A* **2012**, *425−426*, 153−160.
(146) Liu, Y.; Dai, H.; Du, Y.; Deng, J.; Zhang, L.; Zhao, Z.; Au, C. T. *J. Catal.* **2012**, *287*, 149−160.
(147) Xu, J.; Liu, J.; Zhao, Z.; Xu, C.; Zheng, J.; Duan, A.; Jiang, G. *J. Catal.* **2011**, *282*, 1−12.

DOI: 10.1021/acscatal.5b01667
ACS Catal. 2015, 5, 6370−6385